

A super-massive Neptune-sized planet

<https://doi.org/10.1038/s41586-023-06499-2>

Received: 15 May 2023

Accepted: 28 July 2023

Published online: 30 August 2023

 Check for updates

Luca Naponiello^{1,2,3,4,✉}, Luigi Mancini^{1,4,5}, Alessandro Sozzetti⁴, Aldo S. Bonomo⁴, Alessandro Morbidelli⁶, Jingyao Dou⁷, Li Zeng^{8,9}, Zoe M. Leinhardt⁷, Katia Biazzo¹⁰, Patricio E. Cubillos^{4,11}, Matteo Pinamonti⁴, Daniele Locci¹², Antonio Maggio¹², Mario Damasso⁴, Antonino F. Lanza¹³, Jack J. Lissauer^{14,15}, Karen A. Collins⁸, Philip J. Carter⁷, Eric L. N. Jensen¹⁶, Andrea Bignamini¹⁷, Walter Boschin^{18,19,20}, Luke G. Bouma²¹, David R. Ciardi²¹, Rosario Cosentino¹⁸, Ian Crossfield²², Silvano Desidera²³, Xavier Dumusque²⁴, Aldo F. M. Fiorenzano¹⁸, Akihiko Fukui^{19,25}, Paolo Giacobbe⁴, Crystal L. Gnilka^{14,21}, Adriano Ghedina¹⁸, Gloria Guilluy⁴, Avet Harutyunyan¹⁸, Steve B. Howell¹⁴, Jon M. Jenkins¹⁴, Michael B. Lund²¹, John F. Kielkopf²⁶, Katie V. Lester¹⁴, Luca Malavolta^{23,27}, Andrew W. Mann²⁸, Rachel A. Matson²⁹, Elisabeth C. Matthews⁵, Domenico Nardiello²³, Norio Narita^{19,25,30}, Emanuele Pace², Isabella Pagano¹³, Enric Pallé^{19,20}, Marco Pedani¹⁸, Sara Seager^{9,31,32,33}, Joshua E. Schlieder³⁴, Richard P. Schwarz⁸, Avi Shporer^{31,33}, Joseph D. Twicken^{14,35}, Joshua N. Winn³⁶, Carl Ziegler³⁷ & Tiziano Zingales^{23,27}

Neptune-sized planets exhibit a wide range of compositions and densities, depending on factors related to their formation and evolution history, such as the distance from their host stars and atmospheric escape processes. They can vary from relatively low-density planets with thick hydrogen–helium atmospheres^{1,2} to higher-density planets with a substantial amount of water or a rocky interior with a thinner atmosphere, such as HD 95338 b (ref. 3), TOI-849 b (ref. 4) and TOI-2196 b (ref. 5). The discovery of exoplanets in the hot-Neptune desert⁶, a region close to the host stars with a deficit of Neptune-sized planets, provides insights into the formation and evolution of planetary systems, including the existence of this region itself. Here we show observations of the transiting planet TOI-1853 b, which has a radius of 3.46 ± 0.08 Earth radii and orbits a dwarf star every 1.24 days. This planet has a mass of 73.2 ± 2.7 Earth masses, almost twice that of any other Neptune-sized planet known so far, and a density of 9.7 ± 0.8 grams per cubic centimetre. These values place TOI-1853 b in the middle of the Neptunian desert and imply that heavy elements dominate its mass. The properties of TOI-1853 b present a puzzle for conventional theories of planetary formation and evolution, and could be the result of several proto-planet collisions or the final state of an initially high-eccentricity planet that migrated closer to its parent star.

TOI-1853 is a dwarf star with a V-band optical brightness of 12.3 magnitudes, located 167 pc from the Sun. It was photometrically monitored by the Transiting Exoplanet Survey Satellite (TESS) space telescope and the analysis of its light curve showed transit-like events compatible with a planet candidate (see Methods section ‘TESS photometric data’), designated as TOI-1853.01, having a short orbital period of 1.24 days and a Neptune-like radius. We ruled out a nearby eclipsing binary (NEB) blend as the potential source of the TOI-1853.01 detection in the wide TESS pixels by monitoring extra transit events with the higher angular resolution of three ground-based telescopes: MuSCAT2, ULMT and LCOGT (see Methods section ‘Ground-based photometric follow-up’). As part of the standard process for validating transiting exoplanets and assessing the possible contamination of companions on the derived planetary radii⁷, we observed TOI-1853 with near-infrared adaptive optics imaging, using the NIRC2 instrument on the Keck II telescope, and with optical speckle imaging, using the ‘Alopeke speckle imaging camera at Gemini North and high-resolution imaging on the 4.1-m Southern Astrophysical Research (SOAR) telescope. No nearby stars

bright enough to markedly dilute the transits were detected within 0.5”, 1” and 3” of TOI-1853 in the Gemini, Keck and SOAR observations, respectively (see Methods section ‘High-resolution imaging’). Using Gaia DR3 data⁸, we also found that the astrometric solution is consistent with the star being single (see Methods section ‘Gaia’).

In the context of the Global Architecture of Planetary Systems programme^{9,10}, we monitored TOI-1853 with the High Accuracy Radial velocity Planet Searcher for the Northern hemisphere (HARPS-N) spectrograph¹¹, at the Telescopio Nazionale Galileo on the island of La Palma, with the aim of measuring variations of its radial velocity (RV), that is, its velocity projected along the line of sight. The HARPS-N data-reduction software pipeline provided wavelength-calibrated spectra (see Methods section ‘Spectroscopic data’), which we used to determine the stellar atmospheric properties. TOI-1853 is a quiet K2 V star with effective temperature $T_{\text{eff}} = 4,985 \pm 70$ K, surface gravity $\log g = 4.49 \pm 0.11$ dex, iron abundance $[\text{Fe}/\text{H}] = 0.11 \pm 0.08$ dex and solar Fe/Si and Mg/Si ratios (see Methods section ‘Stellar analysis’). Furthermore, we determined a mass of $M_* = 0.837 \pm 0.039$ solar masses (M_{\odot}), a radius of

Table 1 | Stellar and planetary properties

Parameters	Nomenclature	Unit	Value
Stellar			
Spectral class			K2.5 V
Right ascension (J2020)	RA		14h 05 min 50.24 s
Declination (J2020)	dec.		+16° 59' 32.53"
B-band magnitude		mag	13.100 ± 0.031
V-band magnitude		mag	12.276 ± 0.092
J-band magnitude		mag	10.582 ± 0.021
H-band magnitude		mag	10.175 ± 0.018
K-band magnitude		mag	10.055 ± 0.019
WISE1-band magnitude		mag	9.997 ± 0.023
WISE2-band magnitude		mag	10.057 ± 0.019
WISE3-band magnitude		mag	9.956 ± 0.054
Parallax	π	mas	6.022 ± 0.016
Distance	d	pc	166.8 ^{+0.9} _{-0.5}
Projected rotational velocity	$v \sin i$	km s ⁻¹	1.3 ± 0.9
Chromospheric activity indicator	$\log R'_{\text{HK}}$	dex	-4.73 ± 0.06
Mass	M_*	M_\odot	0.837 ± 0.039
Radius	R_*	R_\odot	0.808 ± 0.013
Luminosity	L_*	L_\odot	0.3696 ± 0.0093
Effective temperature	T_{eff}	K	4,985 ± 70
Surface gravity	$\log g$	dex	4.49 ± 0.11
Iron abundance	[Fe/H]	dex	0.11 ± 0.08
Magnesium abundance	[Mg/H]	dex	0.09 ± 0.06
Silicon abundance	[Si/H]	dex	0.14 ± 0.06
Planetary			
Orbital period	P	days	1.2436258 ^{+0.0000015} _{-0.0000015}
RV semi-amplitude	K	ms ⁻¹	48.8 ^{+1.1} _{-1.0}
Eccentricity	e		<0.03
Argument of periastron	ω	°	Unconstrained
Impact parameter	b		0.52 ^{+0.04} _{-0.04}
Reference epoch of mid-transit	T_0	BJD _{TDB}	2459690.7420 ± 0.0006
Transit duration	T_{14}	h	1.19 ± 0.03
Orbital semimajor axis	a	AU	0.0213 ± 0.0005
Orbital inclination	i	°	84.7 ^{+0.4} _{-0.4}
Mass	M_p	M_\oplus	73.2 ^{+2.7} _{-2.7}
Radius	R_p	R_\oplus	3.46 ± 0.08
Density	ρ_p	g cm ⁻³	9.74 ^{+0.82} _{-0.76}
Surface gravity	g	ms ⁻²	60.1 ^{+3.8} _{-3.6}
Equilibrium temperature	T_{eq}	K	1,479 ± 25

The uncertainties represent the 68% confidence intervals (one standard deviation or σ) for each value. The equilibrium temperature is estimated for a zero Bond albedo, in the assumption of uniform heat redistribution to the nightside. The eccentricity upper limit is constrained at the confidence level of 3 σ .

$R_* = 0.808 \pm 0.013$ solar radii (R_\odot) and an advanced, although uncertain, stellar age of $7.0^{+4.6}_{-4.3}$ Gyr (Table 1). We computed the generalized Lomb–Scargle (GLS) periodogram of the HARPS-N RVs and found a substantial peak (with false alarm probability (FAP) $\ll 0.1\%$) at a frequency of about 0.8 per day that matches the transit period and the phase of the planet candidate (see Methods section ‘RV and activity indicators periodograms’). To determine the main physical and orbital parameters of

the system, we performed a global transit and RV joint analysis (see Methods section ‘Joint transit and RV analysis’). Figure 1 shows both the TESS photometric light curve and the HARPS-N RV data, as a function of time and orbital phase. We measured the radius of the companion to be 3.46 ± 0.08 Earth radii (R_\oplus), with a mass of 73.2 ± 2.7 Earth masses (M_\oplus), thus confirming the planetary nature of TOI-1853.01, hereafter TOI-1853 b. These values imply a bulk density of $9.74^{+0.82}_{-0.76}$ g cm⁻³ (roughly six times that of Neptune) and surface gravity of $g_p = 60.1^{+3.8}_{-3.6}$ m s⁻² (about 5.5 times that of Neptune), as detailed in Table 1. Despite its short orbital period, TOI-1853 b may survive during the remaining main-sequence lifetime of its host star (see Methods section ‘Orbital decay’).

The exceptional properties of TOI-1853 b are clearly evident in comparison with the known exoplanet population at present (Fig. 2). Objects with the same density as TOI-1853 b are rare, typically super-Earths, whereas planets with the same mass usually have radii more than twice as large. Furthermore, it occupies a region of the mass–orbital period space of hot planets that was previously devoid of objects, corresponding to the driest area of the hot-Neptune desert¹². TOI-1853 b is twice as massive as the two runners-up with similar radius in the radius–mass diagram (Fig. 2), that is, the ultra-hot ($P = 0.76$ days) Neptune-sized TOI-849 b (ref. 4) and the warm ($P = 55$ days) Neptune HD 95338 b (ref. 3). Although for HD 95338 b and TOI-849 b the atmospheric mass fraction is expected to be at most about 5–7% (ref. 13) and about 4% (ref. 4), respectively, TOI-1853 b is best described as a bare core of half water and half rock with no or negligible envelope, or as having at most 1% atmospheric H/He mass fraction on top of a 99% Earth-like rocky interior (Fig. 2) (see Methods section ‘Composition’).

The characteristic pressure of its deep interior is estimated to reach around 5,000 GPa (50 times the core–mantle boundary pressure of Earth), at which most elements and their compounds are expected to metalize owing to the reduced spacings of neighbouring atoms under extreme compression. The metallic core of TOI-1853 b could be surrounded by a mantle of H₂O in a high-pressure ice phase and, possibly, in the supercritical fluid form¹⁴. However, the properties of matter at such high central pressures are still uncertain and compositional mixing^{15–18} might be present rather than distinct layers, as postulated by standard models^{19,20}. If TOI-1853 b is a water-rich world, its upper structure could be described in terms of a hydrosphere with variable mass fractions of supercritical water on top of a mantle-like interior²¹. Although existing structural models of Neptunes addressing this possibility do not encompass objects with a mass similar to that of TOI-1853 b, atmospheric characterization measurements with the James Webb Space Telescope (JWST) might be telling. For instance, by combining three secondary-eclipse observations with the NIRSpec/G395H instrument, we could constrain the CO₂ absorption feature at 4.5 μm , whose strength is a tracer of atmospheric metallicity. Transmission observations are more challenging; however, NIRISS/SOSS might be able to detect the series of H₂O absorption bands in the 0.9–2.8- μm range, which would distinguish a thin H₂-dominated atmosphere from an H₂O-dominated atmosphere (see Methods section ‘Spectral atmospheric characterization prospects’).

Explaining the formation of such a planet is challenging because of the substantial abundance of heavy elements involved. Pebble accretion, which is the most efficient growth process for massive planets, shuts off when the core is massive enough to disrupt the gas disk²², and accreting solids beyond this mass requires a different process. The planetesimal isolation mass for runaway growth²³ as well as post-isolation growth²⁴ would require exceedingly and unrealistically high surface densities to grow a planet composed almost entirely of condensable material in situ. Thus, the growth of a planet such as TOI-1853 b by planetesimal accretion alone seems unrealistic as well. One possibility is that a system of small planets migrated from the distant regions of the disk towards its inner edge, which could have loaded the inner

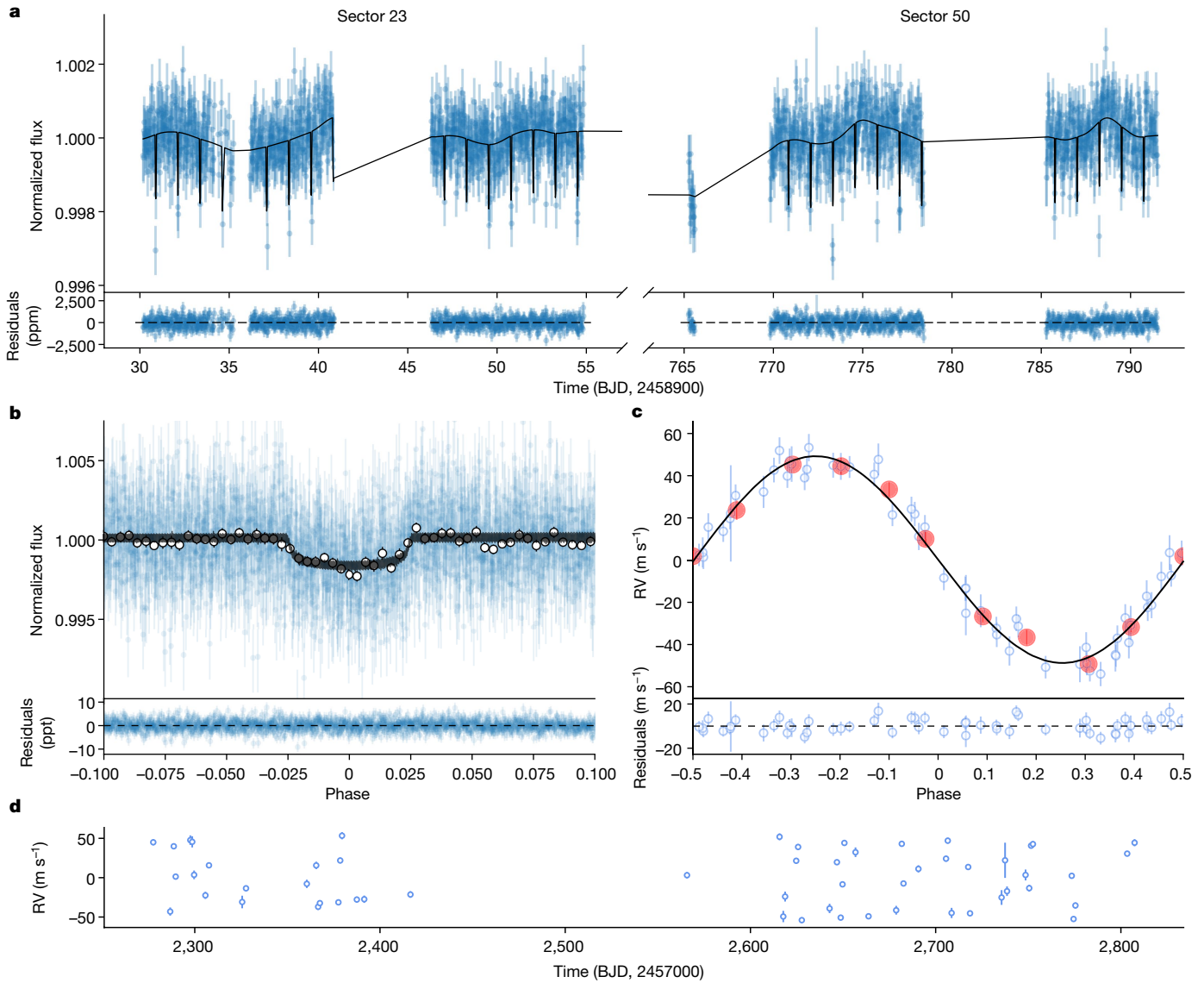


Fig. 1 | Light curve and RVs. **a**, TESS light curve of TOI-1853. **b**, Phase curve of all TESS transits fitted separately. **c**, Phase curve of all the RVs. **d**, HARPS-N RVs. The light curves are binned at a 30-min cadence for clarity. Data points marked with anomaly flags (that is, Coarse Point, Straylight, Impulsive Outliers and Desaturation Events) were excluded from the light curve. In **c**, the average of

approximately six RV measurements are indicated by red dots. In all panels, the error bars represent one standard deviation and in **a–c**, the best-fitting model is shown in black along with its residuals underneath. ppm, parts per million; ppt, parts per thousand.

disk of solid mass. After the disappearance of gas from the disk, the system became unstable, leading to several mutual collisions among the small planets and eventually forming a planet with a large mass of heavy elements, by growth-dominated collisions (Fig. 3). A preliminary, indicative simulation (see Methods section ‘Formation simulations’) shows that the formation of a planet with a large mass of heavy elements by accreting several solid-rich planets is possible, even though growth into a single planet in the system is an unlikely event. More detailed hydrodynamic simulations also suggest that a final high-speed giant impact between two massive proto-planets is needed to account for the atmosphere-poor structure of TOI-1853 b (see Methods section ‘Detail impact simulations’). Moreover, groups of small planets carrying cumulatively about $100 M_{\oplus}$ in proto-planetary disks might be rare, although the Kepler Mission results indicate that this scenario is not unrealistic²⁵.

Another possible formation scenario is based on the jumping model²⁶, in which at least three giant planets form at a few astronomical units from their parent star. After the disappearance of the disk, this

system becomes unstable and suffers mutual scattering, leading to high-eccentricity orbits for the surviving planets, which can then be circularized by tidal damping at perihelion passages. If the inner disk initially contained a lot of solid mass, in the form of planetesimals or small proto-planets, the innermost planet would have engulfed a large fraction of it near perihelion (Fig. 3). To test this possibility, we simulated an eccentric Jupiter-mass planet with an initial budget of 20 to 40 M_{\oplus} in heavy elements and found that it can accrete an extra 30–40 M_{\oplus} (see Methods section ‘Formation simulations’). Then, we investigated the evolutionary history of the atmosphere and concluded that the structure of the current planet cannot be the result of photoevaporation processes owing to the high surface gravity, but might be the result of Roche lobe overflow (RLO)¹² (see Methods section ‘Atmospheric evaporation’). Thus, an initially massive H/He-dominated giant planet TOI-1853 b could have lost the bulk of its envelope mass because of tidal stripping²⁷ near periastron passage during the high-eccentricity migration. The planet that we see now may have survived very close passages to its parent star from early in

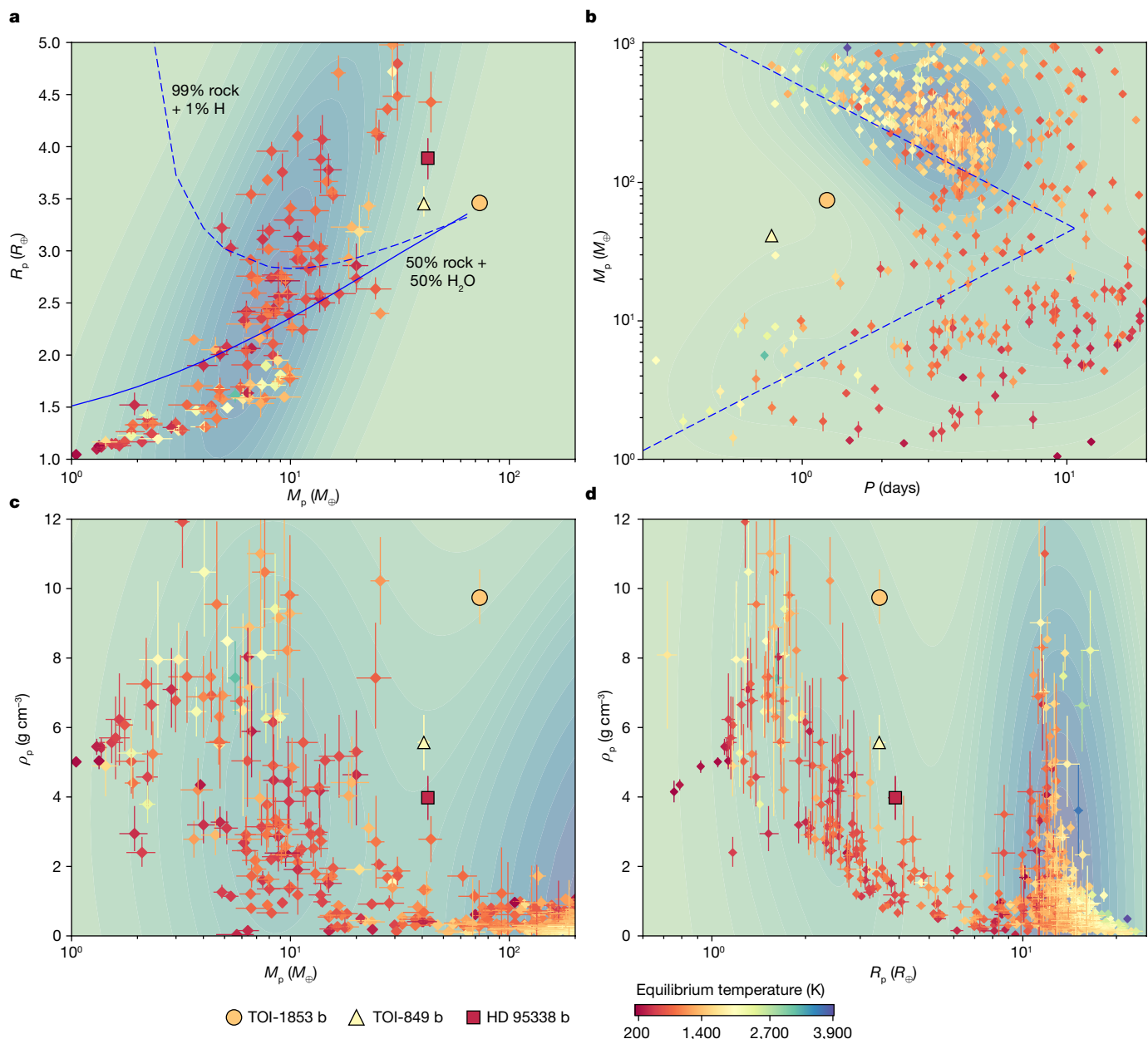


Fig. 2 | Diagrams of known transiting exoplanets. The properties of known exoplanets have been extracted from TEPcat²⁹ and shown as diamonds, their colour being associated with their equilibrium temperature. Horizontal and vertical error bars represent one standard deviation. TOI-1853 b, TOI-849 b and HD 95338 b are shown as circles, triangles and squares, respectively. **a**, Radius–mass diagram with blue lines representing different internal compositions

(dashed line, 99% Earth-like rocky interior + 1% H layer (at temperature and pressure of 1,000 K and 1 mbar, respectively); solid line, 50% Earth-like + 50% water). **b**, Period–mass diagram, in which the dashed blue line encloses the Neptunian desert⁶ ($P_{\text{orb}} \approx 55$ days for HD 95338 b). **c**, Mass–density diagram. **d**, Radius–density diagram.

the history of the system, as the host star would have shrunk to a size of less than $2 R_{\odot}$ well before reaching the main sequence. Tidal heating of a young giant planet still hot from accretion would have further expanded its envelope, facilitating the escape of light gases from the original atmosphere^{12,27,28}.

In any case, the anomalous mass–radius and mass–period combinations of TOI-1853 b are challenging to explain with conventional models of planet formation and evolution. The local merging of solid-rich proto-planets rarely develops into a single planet, whereas the migration scenario would have removed all objects within about 1 AU, so we computed the sensitivity limits of HARPS-N RVs to other planetary companions (see Methods section ‘RV detection function’) and found that we can only exclude, with a 90% confidence level, the presence of companions of masses $>10 M_{\oplus}$ up to orbital periods of $\lesssim 10$ days and

with masses $>30 M_{\oplus}$ up to $\lesssim 100$ days (or about 0.4 AU). Further RV monitoring is thus needed to firmly exclude the presence of other planets within about 1 AU to constrain TOI-1853 b formation, whereas future atmospheric characterization attempts could decipher its composition, allowing us to unveil the history of the densest Neptune-sized planet known at present.

Online content

Any methods, additional references, Nature Portfolio reporting summaries, source data, extended data, supplementary information, acknowledgements, peer review information; details of author contributions and competing interests; and statements of data and code availability are available at <https://doi.org/10.1038/s41586-023-06499-2>.

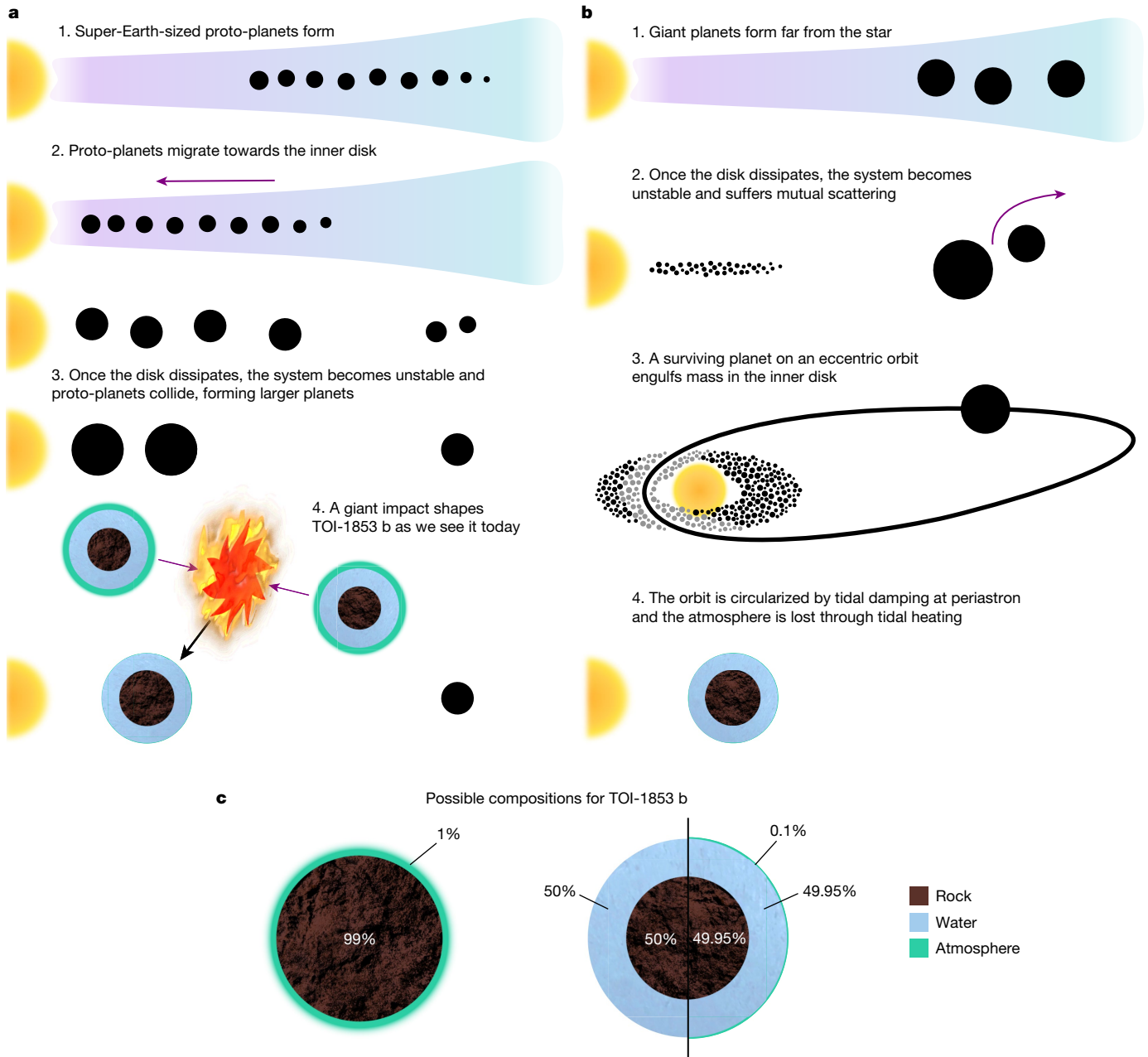


Fig. 3 | Formation scenarios. Two possible pathways for the formation of TOI-1853 b are shown. **a**, The merging of super-Earth-sized proto-planets ends up in a giant collision, generating with high probability a planetary companion within about 1 AU. **b**, Distant giant planets undergo mutual scattering after the

disk dissipation and the surviving one eventually settles into a highly elliptical orbit. Over time, tidal stripping causes the planet to lose its atmosphere and tidal damping at periastron circularizes its orbit. **c**, Both pathways eventually lead to TOI-1853 b, for which three probable compositions are shown.

1. Cubillos, P. et al. An overabundance of low-density Neptune-like planets. *Mon. Not. R. Astron. Soc.* **466**, 1868–1879 (2017).
2. Leleu, A. et al. Removing biases on the density of sub-Neptunes characterised via transit timing variations. Update on the mass-radius relationship of 34 Kepler planets. *Astron. Astrophys.* **669**, A117 (2023).
3. Diaz, M. R. et al. The Magellan/PFS Exoplanet Search: a 55-d period dense Neptune transiting the bright ($V = 8.6$) star HD 95338. *Mon. Not. R. Astron. Soc.* **496**, 4330–4341 (2020).
4. Armstrong, D. J. et al. A remnant planetary core in the hot-Neptune desert. *Nature* **583**, 39–42 (2020).
5. Persson, C. M. et al. TOI-2196 b: rare planet in the hot Neptune desert transiting a G-type star. *Astron. Astrophys.* **666**, 39–42 (2022).
6. Mazeh, T. et al. Dearth of short-period Neptunian exoplanets: a desert in period-mass and period-radius planes. *Astron. Astrophys.* **589**, A75 (2016).
7. Ciardi, D. R. et al. Understanding the effects of stellar multiplicity on the derived planet radii from transit surveys: implications for Kepler, K2, and TESS. *Astrophys. J.* **805**, 16 (2015).
8. Gaia Collaboration. Gaia Early Data Release 3. Summary of the contents and survey properties. *Astron. Astrophys.* **649**, A1 (2021).
9. König, P. C. et al. A warm super-Neptune around the G-dwarf star TOI-1710 revealed with TESS, SOPHIE, and HARPS-N. *Astron. Astrophys.* **666**, A183 (2022).
10. Naponiello, L. et al. The GAPS programme at TNG. XL. A puffy and warm Neptune-sized planet and an outer Neptune-mass candidate orbiting the solar-type star TOI-1422. *Astron. Astrophys.* **667**, A8 (2022).
11. Cosentino, R. et al. Harps-N: the new planet hunter at TNG. *Proc. SPIE* **8446**, 657–676 (2012).
12. Owen, J. E. & Lai, D. Photoevaporation and high-eccentricity migration created the sub-Jovian desert. *Mon. Not. R. Astron. Soc.* **479**, 5012–5021 (2018).
13. Kubyskhina, D. & Fossati, L. The mass-radius relation of intermediate-mass planets outlined by hydrodynamic escape and thermal evolution. *Astron. Astrophys.* **668**, A178 (2022).
14. Zeng, L. et al. New perspectives on the exoplanet radius gap from a Mathematica tool and visualized water equation of state. *Astrophys. J.* **923**, 247 (2021).
15. Bodenheimer, P. et al. New formation models for the Kepler-36 system. *Astrophys. J.* **868**, 138 (2018).
16. Vazan, A. et al. A new perspective on the interiors of ice-rich planets: ice-rock mixture instead of ice on top of rock. *Astrophys. J.* **926**, 150 (2022).
17. Kovačević, T. et al. Miscibility of rock and ice in the interiors of water worlds. *Sci. Rep.* **12**, 13055 (2022).

18. Stevenson, D. J. et al. Mixing of condensable constituents with H–He during the formation and evolution of Jupiter. *Planet. Sci. J.* **3**, 74 (2022).
19. Dorn, C. et al. A generalized Bayesian inference method for constraining the interiors of super Earths and sub-Neptunes. *Astron. Astrophys.* **597**, A37 (2017).
20. Zeng, L. et al. Growth model interpretation of planet size distribution. *Proc. Natl Acad. Sci. USA* **116**, 9723–9728 (2019).
21. Mousis, O. et al. Irradiated ocean planets bridge super-Earth and sub-Neptune populations. *Astrophys. J. Lett.* **896**, L22 (2020).
22. Lambrechts, M. & Johansen, A. Forming the cores of giant planets from the radial pebble flux in protoplanetary discs. *Astron. Astrophys.* **572**, A107 (2014).
23. Safronov, V. S. *Evolution of the Protoplanetary Cloud and Formation of the Earth and the Planets* (Keter, 1972).
24. Lissauer, J. J. Timescales for planetary accretion and the structure of the protoplanetary disk. *Icarus* **69**, 249–265 (1987).
25. Sun, L. et al. Kepler-411: a four-planet system with an active host star. *Astron. Astrophys.* **624**, A15 (2019).
26. Beaugé, C. & Nesvorný, D. Multiple-planet scattering and the origin of hot Jupiters. *Astrophys. J.* **751**, 119 (2012).
27. Beaugé, C. & Nesvorný, D. Emerging trends in a period–radius distribution of close-in planets. *Astrophys. J.* **763**, 12 (2013).
28. Owen, J. E. Atmospheric escape and the evolution of close-in exoplanets. *Annu. Rev. Earth Planet. Sci.* **47**, 67–90 (2019).
29. Southworth, J. Homogeneous studies of transiting extrasolar planets - IV. Thirty systems with space-based light curves. *Mon. Not. R. Astron. Soc.* **417**, 2166–2196 (2011).

Publisher's note Springer Nature remains neutral with regard to jurisdictional claims in published maps and institutional affiliations.

Springer Nature or its licensor (e.g. a society or other partner) holds exclusive rights to this article under a publishing agreement with the author(s) or other rightsholder(s); author self-archiving of the accepted manuscript version of this article is solely governed by the terms of such publishing agreement and applicable law.

© The Author(s), under exclusive licence to Springer Nature Limited 2023, corrected publication 2023

¹Department of Physics, University of Rome “Tor Vergata”, Rome, Italy. ²Department of Physics and Astronomy, University of Florence, Florence, Italy. ³Department of Physics, Sapienza University of Rome, Rome, Italy. ⁴INAF – Turin Astrophysical Observatory, Pino Torinese, Italy. ⁵Max Planck Institute for Astronomy, Heidelberg, Germany. ⁶Laboratoire Lagrange, Université Côte d’Azur, CNRS, Observatoire de la Côte d’Azur, Nice, France. ⁷School of Physics, H.H. Wills Physics Laboratory, University of Bristol, Bristol, UK. ⁸Center for Astrophysics, Harvard & Smithsonian, Cambridge, MA, USA. ⁹Department of Earth and Planetary Sciences, Harvard University, Cambridge, MA, USA. ¹⁰INAF – Rome Astronomical Observatory, Monte Porzio Catone, Italy. ¹¹Space Research Institute, Austrian Academy of Sciences, Graz, Austria. ¹²INAF – Palermo Astronomical Observatory, Palermo, Italy. ¹³INAF – Catania Astrophysical Observatory, Catania, Italy. ¹⁴NASA Ames Research Center, Moffett Field, CA, USA. ¹⁵Department of Earth and Planetary Sciences, Stanford University, Stanford, CA, USA. ¹⁶Department of Physics & Astronomy, Swarthmore College, Swarthmore, PA, USA. ¹⁷INAF – Trieste Astronomical Observatory, Trieste, Italy. ¹⁸Fundación Galileo Galilei - INAF, Tenerife, Spain. ¹⁹Instituto de Astrofísica de Canarias (IAC), Tenerife, Spain. ²⁰Departamento de Astrofísica, Universidad de La Laguna (ULL), Tenerife, Spain. ²¹NASA Exoplanet Science Institute – Caltech/IPAC, Pasadena, CA, USA. ²²Department of Physics and Astronomy, University of Kansas, Lawrence, KS, USA. ²³INAF – Padova Astronomical Observatory, Padova, Italy. ²⁴Observatoire de Genève, Université de Genève, Versoix, Switzerland. ²⁵Komaba Institute for Science, The University of Tokyo, Tokyo, Japan. ²⁶Department of Physics and Astronomy, University of Louisville, Louisville, KY, USA. ²⁷Department of Physics and Astronomy, University of Padova, Padova, Italy. ²⁸Department of Physics and Astronomy, The University of North Carolina at Chapel Hill, Chapel Hill, NC, USA. ²⁹United States Naval Observatory, Washington, DC, USA. ³⁰Astrobiology Center, Osawa, Mitaka, Japan. ³¹Department of Physics, Massachusetts Institute of Technology, Cambridge, MA, USA. ³²Department of Aeronautics and Astronautics, Massachusetts Institute of Technology, Cambridge, MA, USA. ³³Kavli Institute for Astrophysics and Space Research, Massachusetts Institute of Technology, Cambridge, MA, USA. ³⁴NASA Goddard Space Flight Center, Greenbelt, MD, USA. ³⁵SETI Institute, Mountain View, CA, USA. ³⁶Department of Astrophysical Sciences, Princeton University, Princeton, NJ, USA. ³⁷Department of Physics, Engineering & Astronomy, Stephen F. Austin State University, Nacogdoches, TX, USA. ³⁸e-mail: inaponiello@roma2.infn.it

Methods

TESS photometric data

The star TIC 73540072, or TOI-1853, was observed by TESS in Sector 23 at 30-min full-frame images cadence in early 2020 and in Sector 50 at a 2-min cadence in early 2022. The transit signal was first identified in the Quick-Look Pipeline (QLP)³⁰ and later promoted to TESS Object of Interest, TOI-1853.01, planet candidate status by the TESS Science Office³¹. The Science Processing Operations Center (SPOC)^{32,33} pipeline retrieved the 2-min Simple Aperture Photometry (SAP) and Presearch Data Conditioning Simple Aperture Photometry (PDC-SAP^{34,35}) light curves. The transit signal was identified through the Transiting Planet Search (TPS^{36,37}) and passed all diagnostic tests in the data validation^{38,39} modules. All TIC objects, other than the target star, were excluded as sources of the transit signal through the difference image centroid offsets³⁸. Here, for the global joint transit–RV analysis of the system, we adopted the PDC-SAP light curves: SPOC for Sector 23 and TESS-SPOC High-Level Science Product (HLSP)³³ for Sector 50, for which, unlike SAP or QLP light curves, long-term trends were already removed using the so-called co-trending basis vectors. The light curve of Sector 23 was supersampled⁴⁰ at 2 min for the global analysis to properly account for the longer cadence compared with Sector 50 and the ground-based follow-up light curves. The transit depths are found to be consistent within different TESS extraction pipelines, including PATHOS⁴¹, and with ground-based photometry.

Ground-based photometric follow-up

The TESS pixel scale is about 21 arcsec per pixel and photometric apertures extend out to several pixels, generally causing several stars to blend in the TESS aperture. To rule out the NEB-blend scenario and attempt to detect the signal on-target, we observed the field as part of the TESS Follow-up Observing Program Sub Group 1 (TFOP⁴²). We observed full transit windows of TOI-1853 b on 25 and 27 May and 27 June 2020, respectively, with the MuSCAT2 imager⁴³ installed at the 1.52-m Telescopio Carlos Sánchez in the Teide Observatory (in g , r , i and z_s bands), with the 0.61-m University of Louisville Manner Telescope (ULMT) located at Steward Observatory (through a Sloan- r' filter) and with the Las Cumbres Observatory Global Telescope (LCOGT⁴⁴) 1.0-m network node at Siding Spring Observatory (through a Sloan- g' band filter). We extracted the photometric data with AstroImageJ (ref. 45) and measured transit depths across several optical bands consistent with an achromatic transit-like event and compatible with TESS well within 1σ . We ruled out an NEB blend as the cause of the TOI-1853 b detection for all the surrounding stars and included the detrended ground-based observations in the global fit (Extended Data Fig. 1).

High-resolution imaging

As part of the standard process for validating transiting exoplanets to assess the possible contamination of bound or unbound companions on the derived planetary radii⁷, we observed TOI-1853 with near-infrared adaptive optics imaging at Keck and with optical speckle imaging at Gemini and SOAR.

We performed observations at the Keck Observatory with the NIRC2 instrument on Keck II behind the natural guide star adaptive optics system⁴⁶ on 28 May 2020 UT in the standard three-point dither pattern. The dither pattern step size was $3''$ and was repeated twice, with each dither offset from the previous dither by $0.5''$. NIRC2 was used in the narrow-angle mode with a full field of view of about $10''$ and a pixel scale of approximately $0.0099442''$ per pixel. The Keck observations were made in the narrowband Br- γ filter ($\lambda_0 = 2.1686$; $\Delta\lambda = 0.0326 \mu\text{m}$) with an integration time of 15 s for a total of 135 s on the target. The final resolutions of the combined dithers were determined from the full width at half maximum (FWHM) of the point spread functions: $0.053''$. The sensitivities of the final combined adaptive optics image (Extended Data Fig. 2) were determined by injecting simulated sources

azimuthally around the primary target every 20° at separations of integer multiples of the central source's FWHM⁴⁷.

We observed TOI-1853 with the 'Alopeke speckle imaging camera at Gemini North^{48,49}, obtaining seven sets of 1,000 frames (10 June 2020 UT), with each frame having an integration time of 60 ms, in each of the instrument's two bands⁵⁰ (centred at 562 nm and 832 nm). The observations of the target reach a sensitivity in the blue channel of 5.2 mag and in the red channel of 6.3 mag at separations of 0.5 arcsec and show no evidence of further point sources. We also searched for stellar companions to TOI-1853 with speckle imaging on the 4.1-m SOAR telescope⁵¹ on 27 February 2021 UT, observing in Cousins- I band, similar to the TESS bandpass. This observation was sensitive to a 4.7-mag fainter star at an angular distance of 1 arcsec from the target (Extended Data Fig. 2).

Gaia

Gaia DR3 astrometry⁸ provides extra information about the possibility of inner companions that may have gone undetected by high-resolution imaging. For TOI-1853, Gaia found a renormalized unit weight error of 1.08, indicating that the Gaia astrometric solution is consistent with the star being single⁴⁸. Also, in the Gaia archive, we identified no sources within 40 arcsec from the target (approximately 7,000 AU at the distance of TOI-1853) and, therefore, no potentially widely separated companions with the same distance and proper motion.

Spectroscopic data

We gathered 56 spectra of TOI-1853 with HARPS-N¹¹ between February 2021 and August 2022 (Extended Data Table 1), within the GAPS programme, and reduced them using the updated online Data Reduction Software v2.3.5 (ref. 52). A different pipeline based on the template-matching technique, TERRA v1.8 (ref. 53), gave comparable errors and resulted in a fully consistent mass determination.

We observed the star in OBJ_AB mode, with fibre A on the target and fibre B on the sky to monitor possible contamination by moonlight, which we deemed negligible⁵⁴. We extracted the RVs by cross-correlating the HARPS-N spectra with a stellar template close to the stellar spectral type. The median (mean) of the formal uncertainties of the HARPS-N RVs is $3.8(4.6) \text{ m s}^{-1}$; the RV scatter of 34 m s^{-1} reduces to 4.5 m s^{-1} after removing the planetary signal. Our observations had average air mass, signal-to-noise ratio and exposure time of 1.25, 18 and 1,200 s, respectively.

Stellar analysis

We derived spectroscopic atmospheric parameters exploiting the co-added spectrum of TOI-1853. In particular, we measured effective temperature (T_{eff}), surface gravity ($\log g$), microturbulence velocity (ξ) and iron abundance ($[\text{Fe}/\text{H}]$) through a standard method based on measurements of equivalent widths of iron lines^{55,56}. We then adopted the grid of model atmospheres⁵⁷ with new opacities and the spectral analysis package MOOG⁵⁸ version 2017. T_{eff} was derived by imposing that the abundance of Fe I is not dependent on the line excitation potentials, ξ by obtaining the independence between Fe I abundance and the reduced iron line equivalent widths and $\log g$ by the ionization equilibrium condition between Fe I and Fe II.

We also computed the elemental abundance of magnesium and silicon, with respect to the Sun⁵⁶, using the same code and grid of models. The elemental ratios $[\text{Mg}/\text{Fe}]$ and $[\text{Si}/\text{Fe}]$ have solar values within the errors, with no evident enrichment in none of these elements with respect to the others. The stellar projected rotational velocity ($v \sin i$) was obtained through the spectral-synthesis technique of three regions around 5,400, 6,200 and 6,700 Å (ref. 56). By assuming a macroturbulence velocity⁵⁹ $v_{\text{macro}} = 1.8 \text{ km s}^{-1}$, we found $v \sin i = 1.3 \pm 0.9 \text{ km s}^{-1}$, which is below the HARPS-N spectral resolution, thus suggesting an inactive, slowly rotating star, unless it is observed nearly pole-on.

Finally, we determined the stellar physical parameters with the EXOFASTv2 tool⁶⁰, which simultaneously adjusts the stellar radius, mass

and age in a Bayesian differential evolution Markov chain Monte Carlo framework⁶¹, through the modelling of the stellar spectral energy distribution (SED) and the use of the MESA Isochrones and Stellar Tracks (MIST)⁶². To sample the stellar SED, we used the APASS Johnson B , V and Sloan g' , r' , i' magnitudes⁶³, the 2-MASS near-infrared J , H and K magnitudes⁶⁴ and the WISE W1, W2, W3 infrared magnitudes⁶⁵. We imposed Gaussian priors on the T_{eff} and $[\text{Fe}/\text{H}]$ as derived from the analysis of the HARPS-N spectra and on the Gaia DR3 parallax 6.0221 ± 0.0159 mas (ref. 66). We used uninformative priors for all of the other parameters, including the V-band extinction A_V , for which we adopted an upper limit of 0.085 from reddening maps⁶⁷. Extended Data Fig. 3 shows the best fit of the stellar SED. In doing so, we derived a mass of $M_* = 0.837 \pm 0.038 M_\odot$, a radius of $R_* = 0.808 \pm 0.009 R_\odot$ and an age of $\tau = 7.0_{-4.3}^{+4.6}$ Gyr. To evaluate the uncertainties inherent in stellar models, we determined the stellar parameters with two further stellar evolutionary tracks, namely, Yonise-Yale⁶⁸ (Y2) and Dartmouth⁶⁹, finding $M_* = 0.835 \pm 0.029 M_\odot$, $R_* = 0.807 \pm 0.009 R_\odot$, $\tau = 8.0_{-4.4}^{+3.8}$ Gyr and $M_* = 0.849 \pm 0.025 M_\odot$, $R_* = 0.792_{-0.004}^{+0.005} R_\odot$, $\tau = 4.6 \pm 2.8$ Gyr, respectively. We then summed in quadrature to the EXOFASTv2 uncertainties on M_* and R_* the standard deviations of $0.009 M_\odot$ and $0.009 R_\odot$ from the MIST, Y2, and Dartmouth stellar models, to obtain the adopted mass and radius of $M_* = 0.837 \pm 0.039 M_\odot$ and $R_* = 0.808 \pm 0.013 R_\odot$.

RV and activity indicators periodograms

Simultaneously with the RVs, we extracted the time series of several stellar activity indices (Extended Data Fig. 4): the FWHM, contrast and bisector span of the cross-correlation function profile, as well as the Mount Wilson index (S_{MW}) and the spectroscopic lines $H\alpha$, Na and Ca. We computed the GLS periodogram, with *astropy* v.4.3.1 (refs. 70,71), for both the RVs and the activity indexes, which can be seen in Extended Data Fig. 4. In the RVs, we found the most notable peak at 1.24 days (FAP $\ll 0.1\%$), that is, the expected transiting period of TOI-1853 b. This signal is not attributable to stellar activity because none of the measured activity indicators shows a similar periodicity or harmonics. Two strong peaks appear at the frequencies of the 1d aliases of the planetary period (for example, $f_{\text{alias}} = f_{\text{1d}} - f_{1.24\text{d}}$, giving rise to a period of $P_{\text{alias}} \approx 5.1$ days), which are no longer seen when the signal of TOI-1853 b is subtracted, along with any other peak with FAP $\lesssim 5\%$. The activity indicators do not show signals with FAP $\geq 0.1\%$.

Joint transit and RV analysis

For the joint transit–RV analysis of TOI-1853 b, we used the modelling tool *juliet*⁷², which makes use of *batman*⁷³ for the modelling of transits, *RadVel*⁷⁴ for the modelling of RVs and correlated variations, which are treated as Gaussian processes with the packages *george*⁷⁵ and *celerite*⁷⁶. We exploited the dynamic nested sampling package, *dynesty*⁷⁷, to compute Bayesian posteriors and evidence (\mathcal{Z}) for the models.

Even though by default the TESS PDC-SAP photometry is already corrected for both dilution from other objects contained within the aperture using the Compute Optimal Apertures module⁷⁸ and substantial systematic errors, we corrected it for minor fluctuations that were still observable in the light curve (Fig. 1). In particular, we normalized it by fitting a simple (approximate) Matérn GP kernel⁷². We also analysed the SPOC SAP photometry^{79,80}, which is not corrected for long trends, and found no substantial change in the transit depths or any conclusive evidence of the stellar rotation period over the brief time coverage of both sectors.

We constructed a transit-light-curve model with the usual planetary orbital parameters: period P , time of inferior conjunction T_0 , eccentricity e and argument of periastron ω through the parametrization $(\sqrt{e}\sin\omega, \sqrt{e}\cos\omega)$ and the mean density of the parent star ρ_* (ref. 72) from our stellar analysis. For the flux of TESS and the on-ground light curves, we included in the global model both offsets and jitter parameters, along with two hyperparameters of the Matérn GP model: σ_{GP} and ρ_{GP} , which are the amplitude and the length scale, respectively, of

the GP used to correct TESS light curves. The impact parameter ($b = (a_p/R_*)\cos i_p$ for a circular orbit) and the planet-to-star radius ratio k were parameterized as (r_1, r_2) (ref. 81). Moreover, here we make use of a limb-darkening parametrization⁸² for the quadratic limb-darkening coefficients ($q_1, q_2 \rightarrow u_1, u_2$), with Gaussian priors⁸³. Then we include the RV model with the usual systemic velocity $\bar{v}_{\text{HARPS-N}}$, jitter $\sigma_{\text{HARPS-N}}$ and the RV signal semi-amplitude K_p .

The priors for all the parameters that are used in the joint analysis along with the estimates of the parameters' posteriors are summarized in Extended Data Table 2 and the posterior distributions of the most relevant sampling parameters are shown as corner plots in Extended Data Fig. 5. The addition of an RV linear term (for example, RV intercept and slope) or RV GP models⁷² with the simple harmonic oscillator, Matérn and quasi-periodic (which had the best result of the three) kernels⁸⁴ did not substantially increase the Bayesian-log evidence or even worsened it ($\Delta \mathcal{Z}_{\text{base}}^{\text{quasi per}} \approx 2$, $\Delta \mathcal{Z}_{\text{base}}^{\text{linear}} \approx -3$), and resulted in an unconstrained value for the GP evolution timescale. The inclusion of a second planet in the model, with a uniform orbital period prior between 2 and 500 days, did not improve the Bayesian-log evidence either ($\Delta \mathcal{Z}_{\text{base}}^{2\text{pl}} \approx 0$), also resulting in an unconstrained value for the period, which is consistent with the observed lack of features in the GLS of the RV residuals after the subtraction of the TOI-1853 b signal. Furthermore, to check for transit-time variations, we ran a simple test in which the orbital period of the transit model was fixed at its best-fitting value, whereas all the transit times were allowed to vary, finding no clear evidence of transit-time variations as all the transit times are compatible with their expected value within roughly 1σ (see Supplementary Materials).

RV detection function

We estimated the detection function of the HARPS-N RV time series by performing injection-recovery simulations, in which synthetic planetary signals were injected in the RV residuals after the subtraction of the TOI-1853 b signal. We simulated signals of further companions in a logarithmic grid of 30×40 in the planetary mass, M_p , orbital period, P , and parameter space respectively covering the ranges 1–1,000 M_\oplus and 0.5–5,000 days. For each location in the grid, we generated 200 synthetic planetary signals, drawing P and M_p from a log-uniform distribution inside the cell, T_0 from a uniform distribution in $[0, P]$ and assuming circular orbits. Each synthetic signal was then added to the RV residuals. We computed the detection function as the recovery rate of these signals, that is, fitting the signals with either a circular-Keplerian orbit or a linear or quadratic trend, to correctly take into account long-period signals that would not be correctly identified as a Keplerian owing to the short time span of the RV observations (500 days). We adopted the Bayesian information criterion (BIC) to compare the fitted planetary model with a constant model: we considered the planetary signal to be notably detected when $\Delta\text{BIC} > 10$ in favour of the planet-induced model. The detection function was then computed as the fraction of detected signals for each element of the grid (Extended Data Fig. 6).

Orbital decay

According to the current tidal theory, tidal inertial waves are at present not excited inside TOI-1853 by planet b because the rotation period of the star is certainly longer than twice the planetary orbital period⁸⁵, whereas tidal gravity waves are not capable of dissipating efficiently in the central region of the star given the relatively low planetary mass⁸⁶. Even assuming a lower limit for the modified tidal quality factor $Q'_* = 10^7$, the remaining lifetime of the planet is about 4 Gyr according to equation (1) of ref. 87, or longer if we take into account equilibrium tides⁸⁸.

The situation is different if the orbital plane of the planet is inclined relative to the stellar equator⁸⁹ because a dynamical obliquity tide is expected to be excited independently of the star rotation period. Such a dynamical tide would produce a fast decay of the obliquity, whereas it is not equally effective in producing a decay of the orbit semimajor axis⁸⁹. Therefore, the effective Q'_* , which rules the orbital decay, can be

assumed to be approximately unaffected by the stellar or planetary obliquities (see, however, section 2.2 of ref. 90 for quantification of how the obliquities affect the evolution of the semimajor axis). On the other hand, assuming $Q'_* \approx 10^6$ for the dynamical obliquity tide, the e-folding damping time of the stellar obliquity would be about 1.6 Gyr, which is much shorter than the estimated age of the system. Therefore, any initial stellar obliquity may have had time to be damped during the lifetime of the system.

Composition

The planet bulk composition was constrained on the basis of mass–radius relations derived in refs. 14,20. For the calculation, we adopted a second-order adapted polynomial equation of state from ref. 91, using equation of state coefficients from ref. 14. This is a robust estimate because any density of a condensed phase (solid or liquid) in the interior of the planet is mostly determined by pressure, which—in this case—is generated by strong self-gravitation and weakly depends on the temperature. We assumed a completely differentiated planet with an iron (Fe) core and a mantle consisting of silicate (MgSiO_3) rock. The rocky interior (Fig. 2) was assumed to be 32.5% Fe plus 67.5% silicates, broadly consistent with cosmic element abundance ratios and those derived from the host-star abundances taken as a proxy for the proto-planetary disk composition (Table 1), which point to Mg:Si:Fe being close to 1:1:1. The H_2 –He gaseous envelope above the rocky interior was assumed to be a cosmic mixture of 75% H_2 and 25% He by mass. Instead, the 50% H_2O curve in Fig. 2 corresponds to an Earth-like composition with exactly equal mass of H_2O on top. The latter component approximates the mixture of (C,N,O,H)-bearing material that condensed beyond the iceline of the proto-planetary disk in a water-dominated mixture of H_2O , NH_3 and CH_4 . Slightly different compositions are compatible with TOI-1853 b as well, for example, a thin H_2 envelope, 0.1% by mass, might be present along with a rocky interior (49.95%) and the H_2O mantle (49.95%). We neglected both the role of miscibility and chemical reactions at the interface between rock and icy material^{16,17} and that of any phase transition between high-pressure ice and supercritical water²¹. Finally, neither of the possible compositions producing the mass–radius curves in Fig. 2 is expected to be primordial for a planet with the mass and radius of TOI-1853 b. Catastrophic events such as the ones we discuss here, that is, several proto-planet collisions at the onset of dynamical instabilities on disk disappearance or tidal disruption in a high-eccentricity migration scenario, must be invoked.

Formation simulations

We simulated systems of two, four and eight solid-rich planets with a total mass of $80 M_\oplus$, using the code `swift symba5` (ref. 92). For the first scenario of merging proto-planets, we placed the innermost planet at 0.02 AU from the star, similar to TOI-1853 b, and the other planets separated by 1.5 mutual Hill radii, to ensure that the system is violently unstable. The initial eccentricities were assumed to be between 0 and 5×10^{-2} and the inclinations between 0 and 1.4° , to ensure that the system evolves in 3D and the collision probability is not artificially enhanced (see Supplementary Materials). The systems with initially two and four proto-planets merged into a single planet with $80 M_\oplus$. The system with eight super-Earths merged into two planets of 50 and $30 M_\oplus$, respectively. We then performed a fourth simulation starting from a system of ten super-Earths of $10 M_\oplus$ each, which led to the formation of two planets of $70 M_\oplus$ and $30 M_\oplus$.

For the second scenario, we simulated a Jupiter-mass planet on an orbit with a semimajor axis at 1 AU, perihelion distance at 0.02 AU and inclination of 10° . The planet is assumed to have a radius of two Jupiter radii, owing to tidal heating at perihelion. We placed test particles in three rings at 0.02–0.06 AU, 0.1–0.3 AU and 0.5–1.5 AU. In a million years, the planet engulfed 30%, 6% and 2% of the particles in the three rings, respectively (see Supplementary Materials). The sharp decay of efficiency with the distance from the star is expected because the

planetesimals are spread over a larger area. However, this means that the planet can accrete an extra 30–40 M_\oplus if there is enough mass in the disk to begin with.

Detailed impact simulations

TOI-1853 b is too massive to have been formed in situ, but a single large impact, or several smaller ones, might have removed its atmosphere and crust during the final stages of formation, thus boosting its density. Here we consider giant impacts between super-Earths (or mini-Neptunes) as a possible explanation for the internal compositions depicted in Fig. 3. If all the pre-impact super-Earths in the system originally had thin atmospheres like Earth, it would be straightforward to form TOI-1853 b with 1% atmosphere on top of a 99% Earth-like rocky interior. However, for pre-impact super-Earths with thick atmospheres, the required impact velocity to remove most of the atmosphere could be as high as three times the mutual escape velocity of the two colliding bodies^{93,94}. A series of high-speed impacts (≥ 2 mutual escape velocity) or one last catastrophic high-speed impact (≥ 3 mutual escape velocity) could expel most of the gaseous envelope. *N*-body simulations show that the impact speeds of similar-sized objects are normally within two times the mutual escape velocity^{95,96}, but given the close distance of TOI-1853 b to its star, high-speed impacts are not impossible. If TOI-1853 b is a half water–half rock planet, the pre-impact mini-Neptunes composition could be very different. A layer of water on top of a planet could greatly enhance the loss efficiency of the atmosphere⁹⁷, but few studies have examined the problem in three dimensions.

To better understand the loss process of volatiles during these collisions, we conducted a series of smoothed particle hydrodynamics impact simulations under different conditions using SWIFT⁹⁸. Assuming that the initial planets have three layers (H/He on top, a water mantle and a rocky interior), we explored three different compositions: water-rich by mass (67.5% water, 22.5% rock, 10% H/He), equal rock and water (45% rock, 45% water, 10% H/He) and rock-rich (67.5% rock, 22.5% water, 10% H/He), with the thermodynamic profiles of the planets generated using WoMa⁹⁹. These conditions were chosen to give a range of reasonable Neptune-like compositions for the precursor planets. The rocky interior, water and atmosphere layers are modelled using the ANEOS forsterite¹⁰⁰, AQUA water¹⁰¹ and a mixture of hydrogen–helium¹⁰² equation of states, respectively. The ANEOS forsterite equation-of-state table was regenerated using ref. 103 with a more dense grid (1,560 grid points for density, 744 grid points for temperature) and higher maximum density (80 g cm^{-3}) to better model the high-pressure and high-density rocky interior. Each initial target contained approximately 10^6 particles and the atmosphere layers were resolved with at least ten particle layers. The most promising impacts were repeated with higher resolution (10^7 particles) to ensure that the post-collision results converged. The mass of the largest post-collision remnant (M_r) was calculated using a known methodology^{104,105}, whereas the maximum smoothing length h_{max} was set to $5 R_\oplus$.

We tested various impact scenarios including head-on and oblique impacts with a pre-impact impactor to target mass ratios ranging from 0.5 to 1 and target masses of 25, 45, 50 and $60 M_\oplus$. In Extended Data Table 3, we provide selected results from impact simulations. We found that head-on (oblique) merging collisions, in which a target and an impactor collide at a speed approximately equal to their mutual escape velocity (simulations 1–3, 5–7 and 9–11 in Extended Data Table 3), would result in the removal of at most 10% (5%) of their atmospheres. Although giant impacts at approximately mutual escape velocity are the most common, they have low atmosphere-removal efficiency and even a series of impacts may not be enough to remove the gaseous envelope completely. Therefore, the system would need to experience a sequence of mid-speed impacts (≥ 1.5 mutual escape velocity, simulations 4, 8 and 12 in Extended Data Table 3) or at least one high-speed impact (≥ 2 mutual escape velocity) during its final formation stage to remove most of the atmosphere. Simulations 16, 17 and 18 in Extended Data Table 3

Article

represent the potential final giant impact leading to the formation of TOI-1853 b, assuming that the target planet with a mass of $60 M_{\oplus}$ was formed by several previous merging collisions that resulted in little or no compositional change.

A high percentage of water on the initial planets would make the removal of the atmosphere more efficient, as water-rich impacts require the lowest impact velocity and have the highest atmosphere loss fraction. Although there is always some loss of water during impacts, the water-loss efficiency is reduced if more water is present on the planet initially. The mass fractions of the rock in the post-collision remnant tend to increase in all three impact composition setups, confirming that rock is less likely to be lost owing to the core being in the centre and being less compressible than water and the atmosphere.

Considering the results shown in Extended Data Table 3, we expect that the post-collision remnant could have half water and half rock (with a very thin or negligible atmosphere) if the initial planets contained more water than in the equal rock and water case (simulation 17 Extended Data Table 3) but not as much as the water-rich planet (simulation 16). If TOI-1853 b is a half-rock and half-water planet, these impact simulations can be used to infer the composition of either the planets before the final impact or the primordial disk that supplied the material from which TOI-1853 b accreted.

Generating a pure-rock post-collision remnant requires a higher impact speed, as the atmosphere-removal efficiency for rock-rich planets is relatively low. Scaling laws⁹³, applied in the mass regime of TOI-1853 b, suggest that the impact energies required to remove a large fraction of the atmosphere will be in the super-catastrophic regime, and the initial planet would need roughly ten times the final mass to produce a rocky planet with a thin atmosphere. Therefore, if TOI-1853 b is mainly composed of rock, then there would need to have been a greater mass budget in the disk initially, as a higher velocity impact would have ejected much more mass. A water-rich composition for TOI-1853 b is probably easier to produce through impacts than a water-free super-Earth composition.

Atmospheric evaporation

We have considered two possible evaporation mechanisms: photoevaporation induced by high-energy irradiation or RLO. At the present age, the Jeans escape parameter ($\propto M_p/R_p T_{\text{eq}}$)¹⁰⁶ resulted in $\Lambda \gtrsim 100$, adopting the planetary parameters in Table 1. Such a high value indicates that the atmosphere of TOI-1853 b is in hydrodynamic stability against photoevaporation, thanks to the deep gravitational potential well of the planet. To explore its evolution, we adapted a numerical code developed for studying single systems^{107,108}, considering the following three scenarios: rocky interior + an H_2 -dominated envelope (1% by mass); 49.95% rocky interior + 49.95% water mantle + 0.1% H_2 -dominated envelope; 50% rocky interior + 50% water mantle and no envelope. For each case, we created a synthetic population of young planets (10 Myr old) with different atmospheric mass fractions, ranging from 0, 0.1% or 1% (depending on the case) to around 75% of the current planetary mass. At any age, the radius of the planet is the sum of a fixed core radius plus a time-dependent envelope radius.

During the evolutionary history, which we followed up to 7 Gyr, planet contraction occurs as a result of gravitational shrinking and to the possible mass loss through atmospheric evaporation. Assuming a Jupiter-like albedo, $A = 0.5$, we found that none of the planets is either initially, or later becomes, hydrodynamically unstable. Larger radii imply lower values of the Jeans escape parameter, but this is compensated by the lower equilibrium temperatures until the host star reaches the main sequence at an age of approximately 200 Myr.

In the extreme case of zero Bond albedo, planets with initial mass $\leq 180 M_{\oplus}$ and $\geq 75 M_{\oplus}$ can be hydrodynamically unstable ($\Lambda < 80$). We explored the cases near the lowest initial mass (about $75 M_{\oplus}$) or the lowest initial value of the Jeans parameter ($\Lambda \approx 60$), but we found that—in

all these cases—the total mass loss and the radius contraction are not sufficient to recover the assumed planetary structure at the current age.

To investigate the possible mass loss owing to RLO, we computed the volume-averaged Roche radius R_1 (ref. 109) during the different evolutionary histories of the planet described above. It always resulted in being larger than $1.8 R_p$ at the start of the evolution ($t = 10$ Myr), for any value of the assumed initial mass. At later ages, the Roche radius tends to increase owing to any possible mechanism of mass loss. For comparison, we evaluated the outer limit of the atmosphere, that is, the so-called exobase ($p_b \approx 10^{-12}$ bar), by scaling the thermal escape parameter¹¹⁰ $\Gamma = GM_p \mu m_H / k T_1 r$, in which $\mu = 2.3$ is the mean molecular weight and $T_1 = T_{\text{eq}}$, assuming an isothermal atmosphere in hydrostatic equilibrium and $r_1 = R_p$ at $p = 1$ bar. We found that the exobase is located at $r_b = 1.1 R_p$ and, hence, always below the Roche radius. Finally, we computed the orbital period at which a planetary companion would begin losing mass as a result of RLO, given by $P_{\text{RL}} = 0.4 \rho^{-1/2}$ days (refs. 111,112), in which ρ is the mean planet density. This critical period always resulted in being shorter than 0.5 days. Assuming that the planet is not migrating during the evolution, the critical period also remains shorter than the orbital period, and hence no RLO should occur. This result is because of the very large density of the planet, with respect to standard models. As a countercheck, we verified that the critical period would become equal to or larger than the orbital period if the past density of the planet was lower than about 0.1 g cm^{-3} . In our grid of models, the planetary radius remains in the range $4\text{--}12 R_{\oplus}$ for envelope mass fractions up to 75% of the current planetary mass, whereas the critical density would require radii from 16 to $25 R_{\oplus}$. We conclude that RLO processes could have contributed to the loss of TOI-1853 b envelope only if the planet was closer to the star in the past, which—for a circular orbit—corresponds to $P_{\text{orb}} \approx 0.5$ days, almost half of the current one. For this to be true, the planet should have later migrated to its current position in agreement with the high-eccentricity formation scenario, for which planets roughly circularize at twice the periastron distance of the initial eccentric orbit.

Spectral atmospheric characterization prospects

We explored whether the JWST is able to detect spectroscopic signatures of a TOI-1853 b-like planet. According to the transit and emission spectroscopic metrics^{113,114}, TOI-1853 b is at the lower end distribution of targets selected for transmission. For emission instead, TOI-1853 b is comparable with the bulk of the selected JWST secondary-eclipse observations (Extended Data Fig. 7).

We generated synthetic spectra for TOI-1853 b using the open-source PYRAT BAY modelling framework¹¹⁵. We considered two extreme cases based on the scenarios previously explored: (1) a planet with a rocky interior and a 1% H_2 atmosphere and (2) a planet with a 50% rocky interior, 40% H_2O mantle and a 10% H_2O supercritical steam atmosphere. Given the lack of atmospheric composition constraints other than the bulk density of the planet, we adopted a generic solar composition with scaled heavy-element metallicities such that we match the atmospheric mass fraction of the H_2 -dominated and the heavy-element-dominated atmosphere. On the basis of the planet's equilibrium temperature, we assumed an isothermal temperature profile for transmission and a radiative-equilibrium profile for emission. We computed the molecular composition assuming thermochemical equilibrium. We considered the main opacity sources expected for exoplanets in the infrared, that is, from molecular line lists^{116,117} (pre-processed with the repack package¹¹⁸), collision-induced absorption^{119,120} and Rayleigh scattering¹²¹. We then simulated JWST transmission and emission observations with PandExo¹²² for all instruments on board.

Extended Data Fig. 7 shows our model spectra of TOI-1853 b along with the simulated JWST observations combining three visits with each instrument to enhance the signal-to-noise ratios. Either transmission or emission spectroscopic characterization efforts will be challenging. According to the adopted synthetic models, NIRISS/SOSS

and NIRSpec/G395H are the most favourable instruments to detect spectral features based on their spectral coverage and signal-to-noise ratios. Furthermore, NIRSpec/G235H provides the best signal-to-noise ratio at approximately 2–3 μm . The transmission spectra present the largest spectral features for metallicities ranging from 0.01 to 50.0 times solar. For larger metallicities, the amplitude of the features starts to flatten as the mean molecular mass of the atmosphere increases. Notable spectral features are the H₂O bands at 1.0–2.5 μm and a strong CO₂ band at 4.5 μm for super-solar metallicities. Certainly, the presence of clouds and hazes would complicate the interpretation of these observations, as they can also flatten the spectral features, although they tend to be more prevalent for lower-temperature atmospheres¹²³. The emission spectra seem to provide more identifiable features than in transmission (as confirmed by the relatively better spectroscopic metric). Under the assumption of equilibrium chemistry, the CO₂ absorption feature at 4.5 μm is the clearer tracer of metallicity, as the abundance of CO₂ increases more steeply with metallicity than other dominant species, such as H₂O.

Data availability

TESS photometric time series can be freely obtained from the Mikulski Archive for Space Telescopes (MAST) archive at <https://exo.mast.stsci.edu/>. All follow-up light-curve data are available on the ExoFOP-TESS website (<https://exofop.ipac.caltech.edu/tess/target.php?id=73540072>). RVs are presented in Extended Data Table 1. The simulation dataset of Methods section ‘Detailed impact simulations’ is available on Zenodo (<https://doi.org/10.5281/zenodo.8033965>)¹²⁴. Source data are provided with this paper.

Code availability

The juliet Python code is open source and available at <https://github.com/nespinoza/juliet>. The PYRAT BAY modelling framework is open source and available at <https://github.com/pcubillos/pyratbay>. astropy is a common core package for astronomy in Python and EXOFASTv2 is a well-known public exoplanet fitting software. swift symba5 is available at <https://github.com/silburt/swifter>. SWIFT is available at www.swift-sim.com. WoMa is available at <https://github.com/srbonilla/WoMa>. The repack package is available at <https://github.com/pcubillos/repack>. PandExo is available at <https://github.com/natashabatalha/PandExo>.

30. Huang, C. X. et al. Photometry of 10 million stars from the first two years of TESS full frame images: part I. *Res. Notes Am. Astron. Soc.* **4**, 204 (2020).
31. Guerrero, N. M. et al. The TESS Objects of Interest Catalog from the TESS Prime Mission. *Astrophys. J.* **254**, 39 (2021).
32. Jenkins, J. M. et al. The TESS science processing operations center. *Proc. SPIE* **9913**, 1232–1251 (2016).
33. Caldwell, D. A. et al. TESS science processing operations center FFI target list products. *Res. Notes Am. Astron. Soc.* **4**, 201, (2020).
34. Stumpe, M. C. et al. Multiscale systematic error correction via wavelet-based bandsplitting in Kepler data. *Publ. Astron. Soc. Pac.* **126**, 100 (2014).
35. Smith, J. C. et al. Kepler presearch data conditioning II - a Bayesian approach to systematic error correction. *Publ. Astron. Soc. Pac.* **124**, 1000 (2012).
36. Jenkins, J. M. The impact of solar-like variability on the detectability of transiting terrestrial planets. *Astrophys. J.* **575**, 493–505 (2002).
37. Jenkins, J. M. et al. in *Kepler Data Processing Handbook* (ed. Jenkins, J. M.) Ch. 9 (NASA Ames Research Center, 2020).
38. Twicken, J. D. et al. Kepler data validation I—architecture, diagnostic tests, and data products for vetting transiting planet candidates. *Publ. Astron. Soc. Pac.* **130**, 064502 (2018).
39. Li, J. et al. Kepler data validation II—transit model fitting and multiple-planet search. *Publ. Astron. Soc. Pac.* **131**, 024506 (2019).
40. Kipping, D. M. Binning is sinning: morphological light-curve distortions due to finite integration time. *Mon. Not. R. Astron. Soc.* **408**, 1758–1769 (2010).
41. Nardiello, D. A PSF-based approach to TESS high quality data of stellar clusters (PATHOS) - I. *Mon. Not. R. Astron. Soc.* **490**, 3806–3823 (2019).
42. Collins, K. TESS Follow-up Observing Program Working Group (TFOP WG) Sub Group 1 (SG1): Ground-based time-series photometry. In *23rd Meeting of the American Astronomical Society* ID140.05 (AAS, 2019).
43. Narita, N. et al. MuSCAT2: four-color simultaneous camera for the 1.52-m Telescopio Carlos Sánchez. *J. Astron. Telesc. Instrum. Syst.* **5**, 015001 (2019).
44. Brown, T. M. et al. Las Cumbres Observatory global telescope network. *Publ. Astron. Soc. Pac.* **125**, 1031–1055 (2013).
45. Collins, K. A., Kielkopf, J. F., Stassun, K. G. & Hessman, F. V. AstrolmageJ: image processing and photometric extraction for ultra-precise astronomical light curves. *Astron. J.* **153**, 77 (2017).
46. Wizinowich, P. et al. First light adaptive optics images from the Keck II telescope: a new era of high angular resolution imagery. *Publ. Astron. Soc. Pac.* **112**, 315–319 (2000).
47. Furlan, E. et al. The Kepler follow-up observation program. I. A catalog of companions to Kepler stars from high-resolution imaging. *Astron. J.* **153**, 71 (2017).
48. Ziegler, C. et al. SOAR TESS survey. I. Sculpting of TESS planetary systems by stellar companions. *Astron. J.* **159**, 19 (2020).
49. Scott, N. J. et al. Twin high-resolution, high-speed imagers for the Gemini telescopes: instrument description and science verification results. *Front. Astron. Space Sci.* **8**, 716560 (2021).
50. Howell, S. B., Everett, M. E., Sherry, W., Horch, E. & Ciardi, D. R. Speckle camera observations for the NASA Kepler mission follow-up program. *Astron. J.* **142**, 19 (2011).
51. Tokovinin, A. Ten years of speckle interferometry at SOAR. *Publ. Astron. Soc. Pac.* **130**, 035002 (2018).
52. Dumusque, X. Extremely precise HARPS-N solar RV to overcome the challenge of stellar signal. Plato Mission Conference 2021. In *PLATO Mission Conference 2021* 106 (2021).
53. Anglada-Escudé, G. The HARPS-TERRA project. I. Description of the algorithms, performance, and new measurements on a few remarkable stars observed by HARPS. *Astrophys. J. Suppl. Ser.* **200**, 15 (2012).
54. Malavolta, L. et al. The Kepler-19 system: a thick-envelope super-Earth with two Neptune-mass companions characterized using radial velocities and transit timing variations. *Astron. J.* **153**, 224 (2017).
55. Biazzo, K. et al. The GAPS programme with HARPS-N at TNG. X. Differential abundances in the XO-2 planet-hosting binary. *Astron. Astrophys.* **583**, A135 (2015).
56. Biazzo, K. et al. The GAPS Programme at TNG. XXXV. Fundamental properties of transiting exoplanet host stars. *Astron. Astrophys.* **664**, A161 (2022).
57. Castellì, F. & Kurucz, R. L. in *Modelling of Stellar Atmospheres* Vol. 210 (eds Piskunov, N., Weiss, W. W. & Gray, D. F.) poster A20 (International Astronomical Union, 2003).
58. Sneden, C. The nitrogen abundance of the very metal-poor star HD 122563. *Astrophys. J.* **184**, 839–849 (1973).
59. Brewer, J. M., Fischer, D. A., Valenti, J. A. & Piskunov, N. Spectral properties of cool stars: extended abundance analysis of 1,617 planet-search stars. *Astrophys. J.* **225**, 32 (2016).
60. Eastman, J. EXOFASTv2: generalized publication-quality exoplanet modeling code. Record ascl:1710.003 (Astrophysics Source Code Library, 2017).
61. Ter Braak, C. J. F. A Markov chain Monte Carlo version of the genetic algorithm Differential Evolution: easy Bayesian computing for real parameter spaces. *Stat. Comput.* **16**, 239–249 (2006).
62. Paxton, B. et al. Modules for Experiments in Stellar Astrophysics (MESA): binaries, pulsations, and explosions. *Astrophys. J.* **220**, 15 (2015).
63. Henden, A. A. et al. AAVSO Photometric All Sky Survey (APASS) DR9 (Henden+, 2016): VizieR Online Data Catalog II/336 (VizieR Online Data Catalog, 2016).
64. Cutri, R. M. et al. *2MASS All Sky Catalog of Point Sources* (NASA/IPAC Infrared Science Archive, 2003).
65. Cutri, R. M. et al. ALLWISE Data Release (Cutri+ 2013): VizieR On-line Data Catalog II/328 (VizieR Online Data Catalog, 2021).
66. Gaia Collaboration. Gaia Data Release 3. Summary of the content and survey properties. *Astron. Astrophys.* **674**, A1 (2023).
67. Schlafly, E. F. & Finkbeiner, D. P. Measuring reddening with Sloan Digital Sky Survey stellar spectra and recalibrating SFD. *Astrophys. J.* **737**, 103 (2011).
68. Demarque, P., Woo, J.-H., Kim, Y.-C. & Yi, S. K. Y² isochrones with an improved core overshoot treatment. *Astrophys. J.* **155**, 667–674 (2004).
69. Dotter, A., Chaboyer, B., Jevremovic, D. & Kostov, V. The Dartmouth stellar evolution database. *Astrophys. J.* **178**, 89–101 (2008).
70. Zechmeister, M. & Kürster, M. The Generalised Lomb-Scargle periodogram. A new formalism for the floating-mean and Keplerian periodograms. *Astron. Astrophys.* **496**, 577–584 (2009).
71. Astropy Collaboration. The Astropy Project: building an open-science project and status of the v2.0 core package. *Astron. J.* **156**, 123 (2018).
72. Espinoza, N., Kossakowski, D. & Brahm, R. juliet: a versatile modelling tool for transiting and non-transiting exoplanetary systems. *Mon. Not. R. Astron. Soc.* **490**, 2262–2283 (2019).
73. Kreidberg, L. batman: BAsic Transit Model cAlculationN in Python. *Publ. Astron. Soc. Pac.* **127**, 1161 (2015).
74. Fulton, B. J., Petigura, E. A., Blunt, S. & Sinukoff, E. RadVel: the radial velocity modeling toolkit. *Publ. Astron. Soc. Pac.* **130**, 044504 (2018).
75. Ambikasaran, S., Foreman-Mackey, D., Greengard, L., Hogg, D. W. & O’Neil, M. Fast direct methods for Gaussian processes. *IEEE Trans. Pattern Anal. Mach. Intell.* **38**, 252–265 (2015).
76. Foreman-Mackey, D., Agol, E., Ambikasaran, S. & Angus, R. Fast and scalable Gaussian process modeling with applications to astronomical time series. *Astron. J.* **154**, 220 (2017).
77. Speagle, J. S. DYNESTY: a dynamic nested sampling package for estimating Bayesian posteriors and evidences. *Mon. Not. R. Astron. Soc.* **493**, 3132–3158 (2020).
78. Bryson, S. T. et al. in *Kepler Data Processing Handbook* (ed. Jenkins, J. M.) Ch. 3 (NASA Ames Research Center, 2020).
79. Twicken, J. D. et al. Photometric analysis in the Kepler Science Operations Center pipeline. *Proc. SPIE* **7740**, 749–760 (2010).
80. Morris, R. L. et al. in *Kepler Data Processing Handbook* (ed. Jenkins, J. M.) Ch. 6 (NASA Ames Research Center, 2020).
81. Espinoza, N. Efficient joint sampling of impact parameters and transit depths in transiting exoplanet light curves. *Res. Notes Am. Astron. Soc.* **2**, 209 (2018).
82. Kipping, D. M. Efficient, uninformative sampling of limb darkening coefficients for two-parameter laws. *Mon. Not. R. Astron. Soc.* **435**, 2152–2160 (2013).

83. Claret, A. Limb and gravity-darkening coefficients for the TESS satellite at several metallicities, surface gravities, and microturbulent velocities. *Astron. Astrophys.* **600**, A30 (2017).
84. Foreman-Mackey, D., Agol, E., Ambikasaran, S. & Angus, R. Fast and scalable Gaussian process modeling with applications to astronomical time series. *Astron. J.* **154**, 220 (2017).
85. Ogilvie, G. I. & Lin, D. N. C. Tidal dissipation in rotating solar-type stars. *Astrophys. J.* **661**, 1180–1191 (2007).
86. Barker, A. J. Tidal dissipation in evolving low-mass and solar-type stars with predictions for planetary orbital decay. *Mon. Not. R. Astron. Soc.* **498**, 2270–2294 (2020).
87. Metzger, B. D., Giannios, D. & Spiegel, D. S. Optical and X-ray transients from planet–star mergers. *Mon. Not. R. Astron. Soc.* **425**, 2778–2798 (2012).
88. Collier Cameron, A. & Jardine, M. Hierarchical Bayesian calibration of tidal orbit decay rates among hot Jupiters. *Mon. Not. R. Astron. Soc.* **476**, 2542–2555 (2018).
89. Lai, D. Tidal dissipation in planet-hosting stars: damping of spin–orbit misalignment and survival of hot Jupiters. *Mon. Not. R. Astron. Soc.* **423**, 486–492 (2012).
90. Leconte, J., Chabrier, G., Baraffe, I. & Levrard, B. Is tidal heating sufficient to explain bloated exoplanets? Consistent calculations accounting for finite initial eccentricity. *Astron. Astrophys.* **516**, A64 (2010).
91. Holzapfel, W. B. Coherent thermodynamic model for solid, liquid and gas phases of elements and simple compounds in wide ranges of pressure and temperature. *Solid State Sci.* **80**, 31–34 (2018).
92. Duncan, M. J., Levison, H. F. & Lee, M. H. A multiple time step symplectic algorithm for integrating close encounters. *Astron. J.* **116**, 2067–2077 (1998).
93. Denman, T. R. et al. Atmosphere loss in planet–planet collisions. *Mon. Not. R. Astron. Soc.* **496**, 1166–1181 (2020).
94. Denman, T. R. et al. Atmosphere loss in oblique Super-Earth collisions. *Mon. Not. R. Astron. Soc.* **513**, 1680–1700 (2022).
95. Chambers, J. E. et al. Late-stage planetary accretion including hit-and-run collisions and fragmentation. *Icarus* **224**, 43–56 (2013).
96. Quintana, E. V. et al. The frequency of giant impacts on Earth-like worlds. *Astron. J.* **821**, 126 (2016).
97. Genda, H. & Abe, Y. Enhanced atmospheric loss on proto-planets at the giant impact phase in the presence of oceans. *Nature* **433**, 842–844 (2005).
98. Schaller, M., Gonnet, P., Chalk, A. B. & Draper, P. W. in *Proc. Platform for Advanced Scientific Computing Conference Article No. 2* (ACM, 2016).
99. Ruiz-Bonilla, S. et al. The effect of pre-impact spin on the Moon-forming collision. *Mon. Not. R. Astron. Soc.* **500**, 2861–2870 (2020).
100. Stewart, S. et al. The shock physics of giant impacts: key requirements for the equations of state. *AIP Conf. Proc.* **2272**, 080003 (2020).
101. Haldemann, J., Alibert, Y., Mordasini, C. & Benz, W. AQUA: a collection of H₂O equations of state for planetary models. *Astron. Astrophys.* **643**, A105 (2020).
102. Hubbard, W. B. & MacFarlane, J. J. Structure and evolution of Uranus and Neptune. *J. Geophys. Res. Solid Earth* **85**, 225–234 (1980).
103. Stewart, S. T. et al. Equation of state model Forsterite-ANEOS-SLTV1.0G1: documentation and comparisons. [Zenodo https://zenodo.org/record/3478631](https://zenodo.org/record/3478631) (2019).
104. Marcus, R. A., Stewart, S. T., Sasselov, D. & Hernquist, L. Collisional stripping and disruption of super-Earths. *Astrophys. J.* **700**, L118–L122 (2009).
105. Carter, P. J., Leinhardt, Z. M., Elliott, T., Stewart, S. T. & Walter, M. J. Collisional stripping of planetary crusts. *Earth Planet. Sci. Lett.* **484**, 276–286 (2018).
106. Fossati, L. et al. Aeronomical constraints to the minimum mass and maximum radius of hot low-mass planets. *Astron. Astrophys.* **598**, A90 (2017).
107. Locci, D., Cecchi-Pestellini, C. & Micela, G. Photo-evaporation of close-in gas giants orbiting around G and M stars. *Astron. Astrophys.* **624**, A101 (2019).
108. Maggio, A. et al. New constraints on the future evaporation of the young exoplanets in the V1298 Tau system. *Astrophys. J.* **925**, 172 (2022).
109. Eggleton, P. Approximations to the radii of Roche lobes. *Astrophys. J.* **268**, 368–369 (1983).
110. Koskinen, T. T. et al. Mass loss by atmospheric escape from extremely close-in planets. *Astrophys. J.* **929**, 52 (2022).
111. Rappaport, S. et al. The Roche limit for close-orbiting planets: minimum density, composition constraints, and application to the 4.2 hr planet KOI 1843.03. *Astrophys. J. Lett.* **773**, L15 (2013).
112. Jackson, B. et al. A new model of Roche lobe overflow for short-period gaseous planets and binary stars. *Astrophys. J.* **835**, 145 (2017).
113. Kempton, E. M.-R. et al. A framework for prioritizing the TESS planetary candidates most amenable to atmospheric characterization. *Publ. Astron. Soc. Pac.* **130**, 114401 (2018).
114. Bean, J. L. et al. The Transiting Exoplanet Community Early Release Science Program for JWST. *Publ. Astron. Soc. Pac.* **130**, 114402 (2018).
115. Cubillos, P. E. & Blecic, J. The PYRAT BAY framework for exoplanet atmospheric modelling: a population study of Hubble/WFC3 transmission spectra. *Mon. Not. R. Astron. Soc.* **505**, 2675–2702 (2021).
116. Rothman, L. S. et al. HITEMP, the high-temperature molecular spectroscopic database. *J. Quant. Spectrosc. Radiat. Transf.* **111**, 2139–2150 (2010).
117. Tennyson, J. et al. The 2020 release of the ExoMol database: molecular line lists for exoplanet and other hot atmospheres. *J. Quant. Spectrosc. Radiat. Transf.* **255**, 107228 (2020).
118. Cubillos, P. E. An algorithm to compress line-transition data for radiative-transfer calculations. *Astrophys. J.* **850**, 32 (2017).
119. Borysow, J., Frommhold, L. & Birnbaum, G. Collision-induced rototranslational absorption spectra of H₂-He pairs at temperatures from 40 to 3000 K. *Astrophys. J.* **326**, 509 (1988).
120. Borysow, A., Jorgensen, U. G. & Fu, Y. High-temperature (1000–7000 K) collision-induced absorption of H₂ pairs computed from the first principles, with application to cool and dense stellar atmospheres. *J. Quant. Spectrosc. Radiat. Transf.* **68**, 235–255 (2001).
121. Kurucz, R. L. *Atlas: A Computer Program for Calculating Model Stellar Atmospheres* SAO Special Report No. 309 (Smithsonian Institution, Astrophysical Observatory, 1970).
122. Batalha, N. E. et al. PandExo: a community tool for transiting exoplanet science with JWST & HST. *Publ. Astron. Soc. Pac.* **129**, 064501 (2017).
123. Morley, C. V. et al. Thermal emission and reflected light spectra of super Earths with flat transmission spectra. *Astrophys. J.* **815**, 110 (2015).
124. Naponiello, L. et al. A super-massive Neptune-sized planet. *Zenodo* <https://doi.org/10.5281/zenodo.8033965> (2023).

Acknowledgements We acknowledge the use of public TESS data from pipelines at the TESS Science Office and at the TESS Science Processing Operations Center. Resources supporting this work were provided by the NASA High-End Computing (HEC) programme through the NASA Advanced Supercomputing (NAS) Division at Ames Research Center for the production of the SPOC data products. The work is based on observations made with the Italian Telescopio Nazionale Galileo (TNG) operated on the island of La Palma by the Fundación Galileo Galilei of the INAF (Istituto Nazionale di Astrofisica) at the Spanish Observatorio del Roque de los Muchachos of the Instituto de Astrofísica de Canarias. This work has also made use of data from the European Space Agency (ESA) mission Gaia (<https://www.cosmos.esa.int/gaia>), processed by the Gaia Data Processing and Analysis Consortium (DPAC; <https://www.cosmos.esa.int/web/gaia/dpac/consortium>). This work makes use of observations from the LCOGT network. Part of the LCOGT telescope time was granted by NOIRLab through the Mid-Scale Innovations Program (MSIP). MSIP is funded by the National Science Foundation (NSF). This research has made use of the Exoplanet Follow-up Observing Program (ExoFOP; <https://doi.org/10.26134/ExoFOP5>) website, which is operated by the California Institute of Technology, under contract with the National Aeronautics and Space Administration under the Exoplanet Exploration Program. This paper makes use of observations made with the MuSCAT2 instrument, developed by the Astrobiology Center at Telescopio Carlos Sánchez operated on the island of Tenerife by the IAC in the Spanish Observatorio del Teide and is also based in part on observations obtained at the Southern Astrophysical Research (SOAR) telescope, which is a joint project of the Ministerio da Ciência, Tecnologia e Inovações do Brasil (MCTI/LNA), the US NSF's NOIRLab, the University of North Carolina at Chapel Hill (UNC) and Michigan State University (MSU). This work has been carried out within the framework of the NCCR PlanetS supported by the Swiss National Science Foundation under grants 51NF40-182901 and 51NF40-205606. This paper made use of observations from the high-resolution imaging instrument 'Alopeco, which were obtained under Gemini LLP proposal number GN/S-2021A-LP-105. 'Alopeco was funded by the NASA Exoplanet Exploration Program and built at the NASA Ames Research Center by S. B. Howell, N. Scott, E. P. Horch and E. Quigley. 'Alopeco was mounted on the Gemini North telescope of the international Gemini Observatory, a programme of the NSF's OIR Lab, which is managed by the Association of Universities for Research in Astronomy (AURA) under a cooperative agreement with the NSF. On behalf of the Gemini partnership: the NSF (United States), National Research Council (Canada), Agencia Nacional de Investigación y Desarrollo (Chile), Ministerio de Ciencia, Tecnología e Innovación (Argentina), Ministério da Ciência, Tecnologia, Inovações e Comunicações (Brazil) and Korea Astronomy and Space Science Institute (Republic of Korea). The giant impact simulations were carried out using the computational facilities of the Advanced Computing Research Centre, University of Bristol. Funding for the DPAC has been provided by national institutions, in particular, the institutions participating in the Gaia Multilateral Agreement. L.N. and D.L. acknowledge the support of the ARIEL ASI-INAF agreement 2021-5-HH.O. L. Mancini acknowledges support from the 'Fondi di Ricerca Scientifica d'Ateneo 2021' of the University of Rome 'Tor Vergata'. A. Maggio and A.S.B. acknowledge support from the ASI-INAF agreement no. 2018-16-HH.O (THE StellarR Path project) and from PRIN INAF 2019. P.E.C. is funded by the Austrian Science Fund (FWF) Erwin Schroedinger Fellowship programme J4595-N. Funding for the TESS mission is provided by NASA's Science Mission Directorate. This project has received funding from the European Research Council (ERC) under the European Union's Horizon 2020 research and innovation programme (grant agreement SCORE no. 851555). S.B.H. acknowledges funding from the NASA Exoplanet Program Office. K.A.C. acknowledges support from the TESS mission through sub-award s3449 from MIT. T.Z. acknowledges support from CHEOPS ASI-INAF agreement no. 2019-29-HH.O. J.D. acknowledges funding support from the Chinese Scholarship Council (no. 202008610218). This work is partly supported by JSPS KAKENHI grant numbers JP17H04574 and JP18H05439 and JST CREST grant number JPMJCR1761. We acknowledge DOE-NNSA grant number DE-NA0004084 to Harvard University: Z Fundamental Science Program.

Author contributions L.N. performed the global transit-RV data analysis and wrote the manuscript. A.S. and A.S.B. performed the selection of TESS Neptunes for the HARPS-N follow-up and scheduled the HARPS-N observations within the GAPS consortium. A.S. performed a preliminary RV analysis. L.M., A.S.B., A.S. and M.D. supervised the work and contributed to writing the manuscript. X.D. reduced HARPS-N spectra with the new Data Reduction Software. M. Pinamonti estimated the detection function of HARPS-N RVs. A.S.B. and K.B. determined the stellar parameters. A.W.M. and C.Z. performed and analysed SOAR observations and J.E.S., S.B.H., K.V.L., C.L.G., E.C.M. and R.A.M. obtained and reduced the Gemini data. D.R.C. and C.Z. contributed to writing the high-resolution imaging section. D.R.C. analysed Keck data. A. Morbidelli performed the simulations and contributed to writing the formation scenario with the help of J.J.L. and J.D., Z.M.L. and P.J.C. computed the body collision simulations. L.Z. and A. Sozzetti analysed the composition of the planet. K.A.C. scheduled the LCO observations, performed data reduction along with R.P.S., and contributed to writing the light-curve follow-up sections. J.F.K. performed the ULMT observations and their data reduction. N.N. and A.F. scheduled the observations of MuSCAT2 and E. Palle obtained the data. E.L.N.J. performed a preliminary joint Markov chain Monte Carlo analysis of the on-ground light curves. D.L. and A. Maggio analysed the evolutionary history of the atmosphere. P.E.C. calculated the synthetic transmission and emission spectral signals from JWST, with the help of G.G. and P.G. A.F.L. computed the lifetime of the planet. S.D., A.B., E. Pace, D.N., I.P., L. Malavolta and T.Z. are members of the Science Team of the GAPS (Global Architecture of Planetary Systems) consortium and are responsible for the observing programme and A.G., R.C., W.B., A.F.M.F., M. Pedani and A.H. are members of the TNG

(Telescopio Nazionale Galileo), which has conducted the RV observations. L.G.B. is a member of the TESS Payload Operations Center (POC) and J.D.T. and J.M.J. are members of the TESS Science Processing Operations Center (SPOC), which delivered TESS light curves. A. Shporer, M.B.L., S.S. and J.N.W. are TESS contributors. All authors have contributed to the interpretation of the data and the results.

Competing interests The authors declare no competing interests.

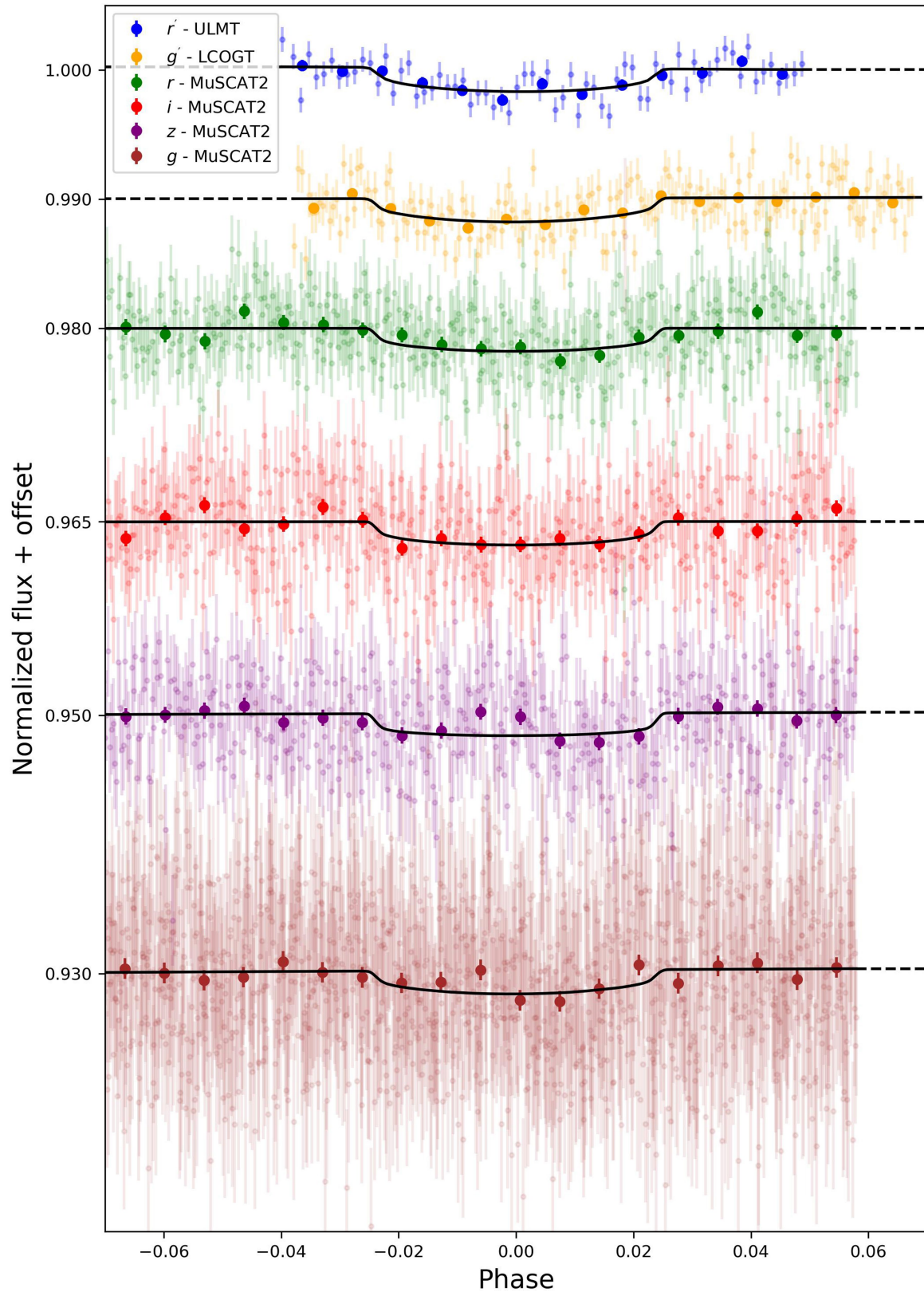
Additional information

Supplementary information The online version contains supplementary material available at <https://doi.org/10.1038/s41586-023-06499-2>.

Correspondence and requests for materials should be addressed to Luca Naponiello.

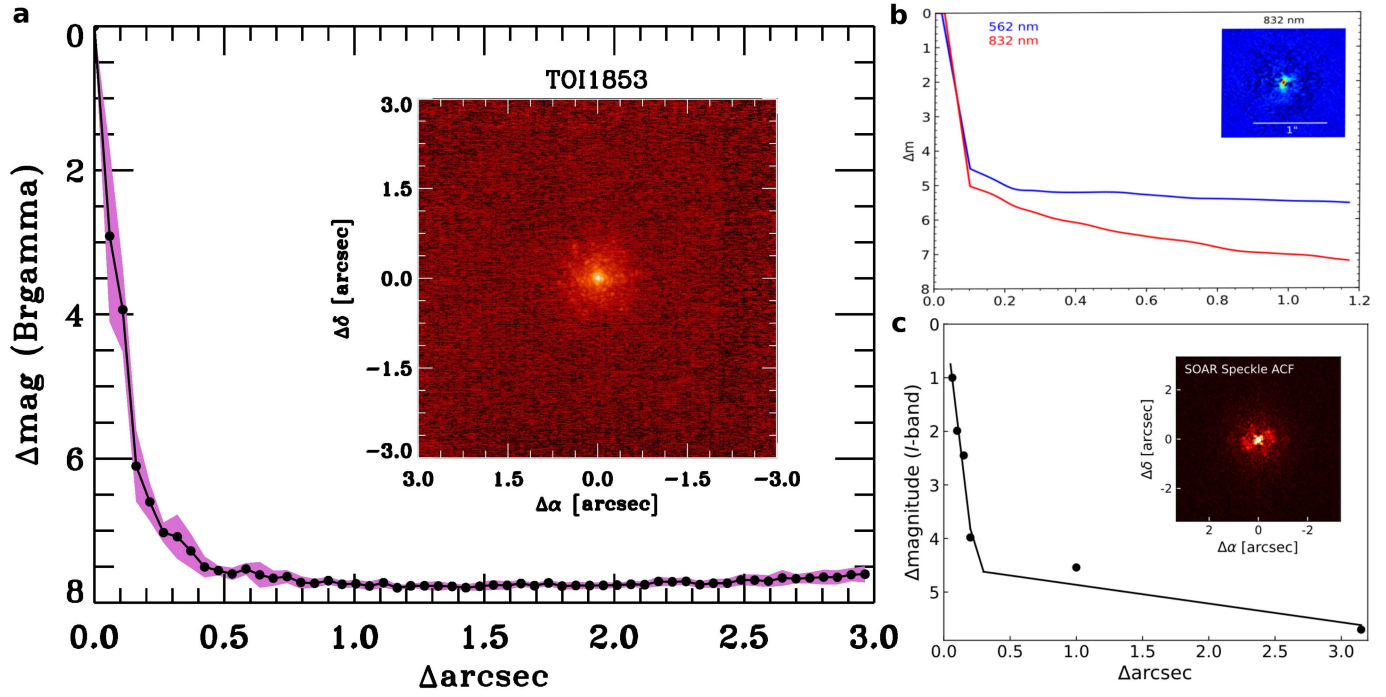
Peer review information *Nature* thanks the anonymous reviewers for their contribution to the peer review of this work.

Reprints and permissions information is available at <http://www.nature.com/reprints>.



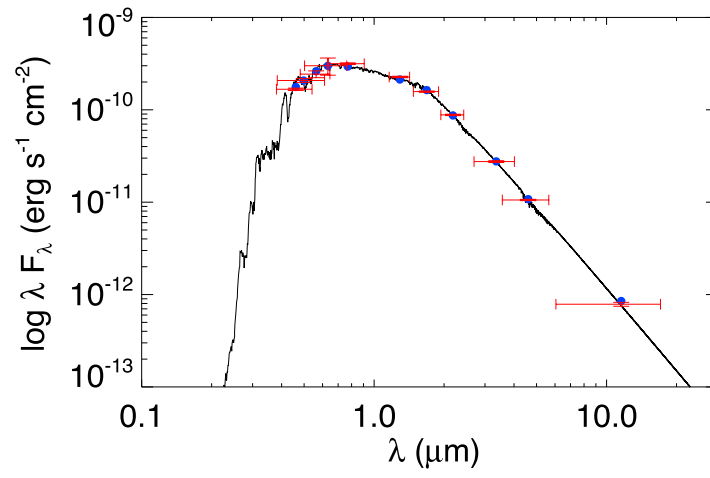
Extended Data Fig. 1 | Global fit result for the ground-based transits. The light curves of MuSCAT2, LCOGT and ULMT have been shifted on the y axis for clarity and their respective filter band is indicated in the legend. The

superimposed points represent approximately 10-min bins, whereas the error bars represent one standard deviation. The global fit from this work is depicted in black.

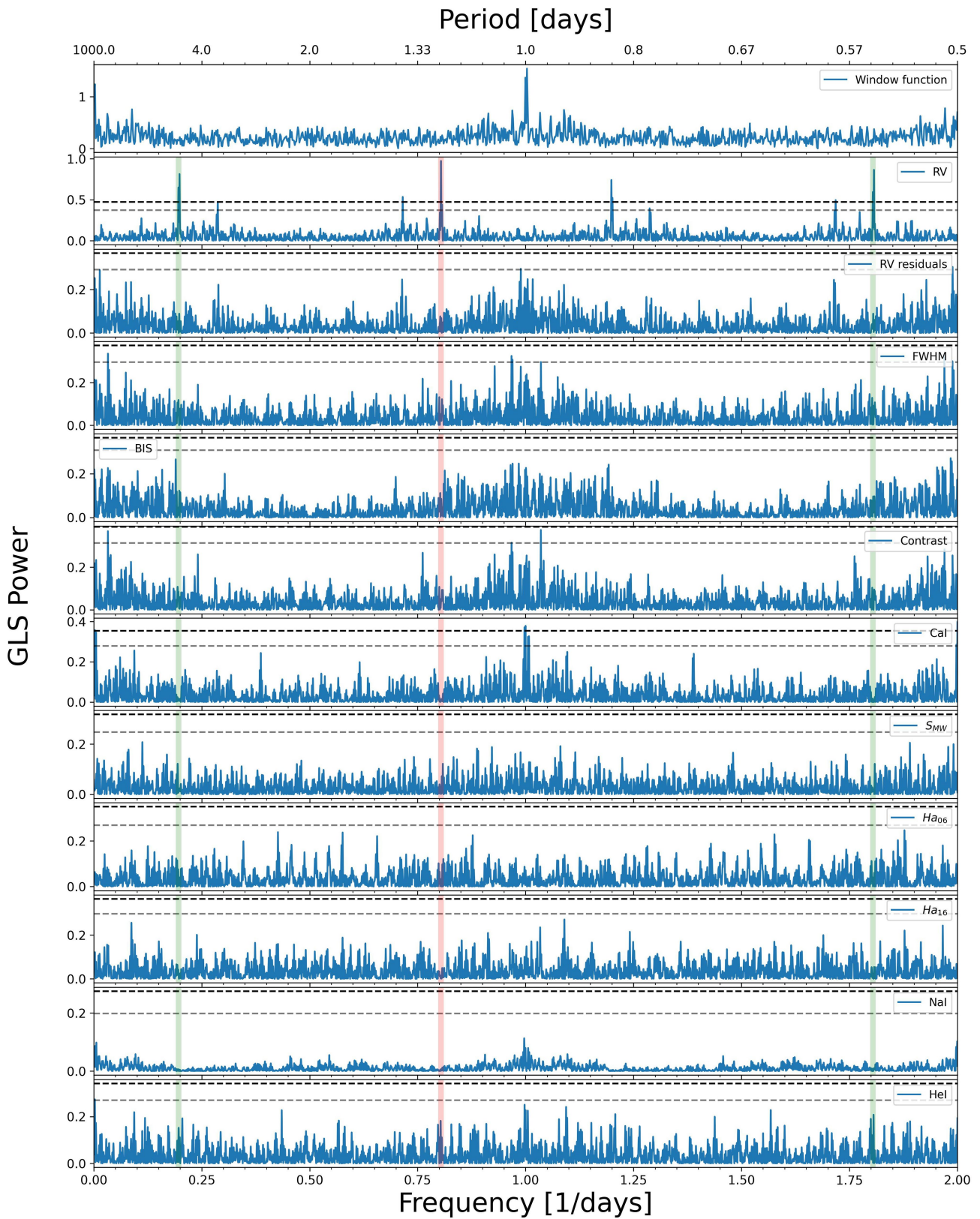


Extended Data Fig. 2 | High-resolution sensitivity curves. Final sensitivity of Keck (a), Gemini (b) and SOAR (c), plotted as a function of angular separation from the host star. The images reach a contrast of about 7.6 (a), about 5.2 and

6.3 (b) and about 4.7 (c) magnitudes fainter than TOI-1853 within 0.5" in each respective band. Images of the central portion of the data are presented as insets in the relative panels.

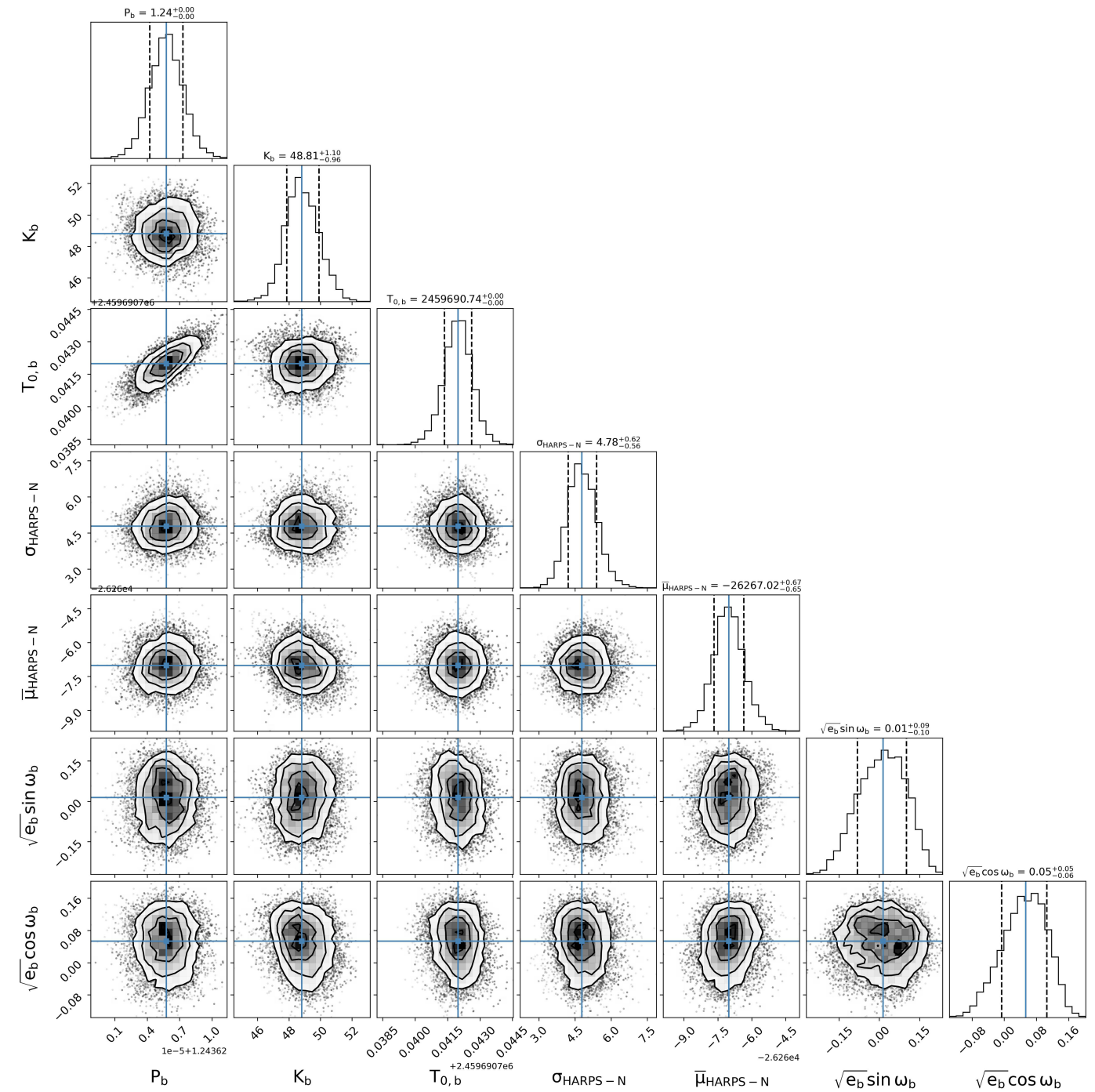


Extended Data Fig. 3 | TOI-1853 spectral energy distribution. The error bars represent one standard deviation. The best-fit model is shown as a solid black line.

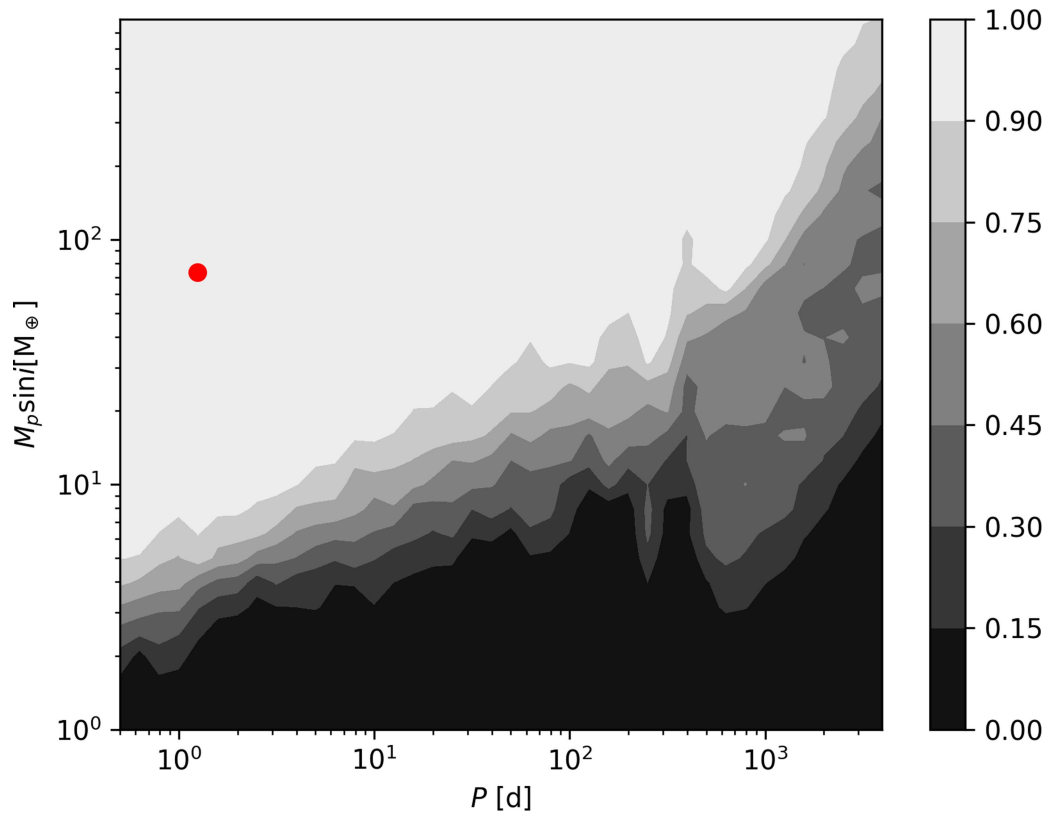


Extended Data Fig. 4 | GLS periodograms. The periodograms of the RVs, its residuals from the global fit and several activity indexes are plotted consecutively. The window function is on top as reference. The main peak of the RV GLS periodogram, at 1.24 days and its 1-day aliases, are highlighted by a

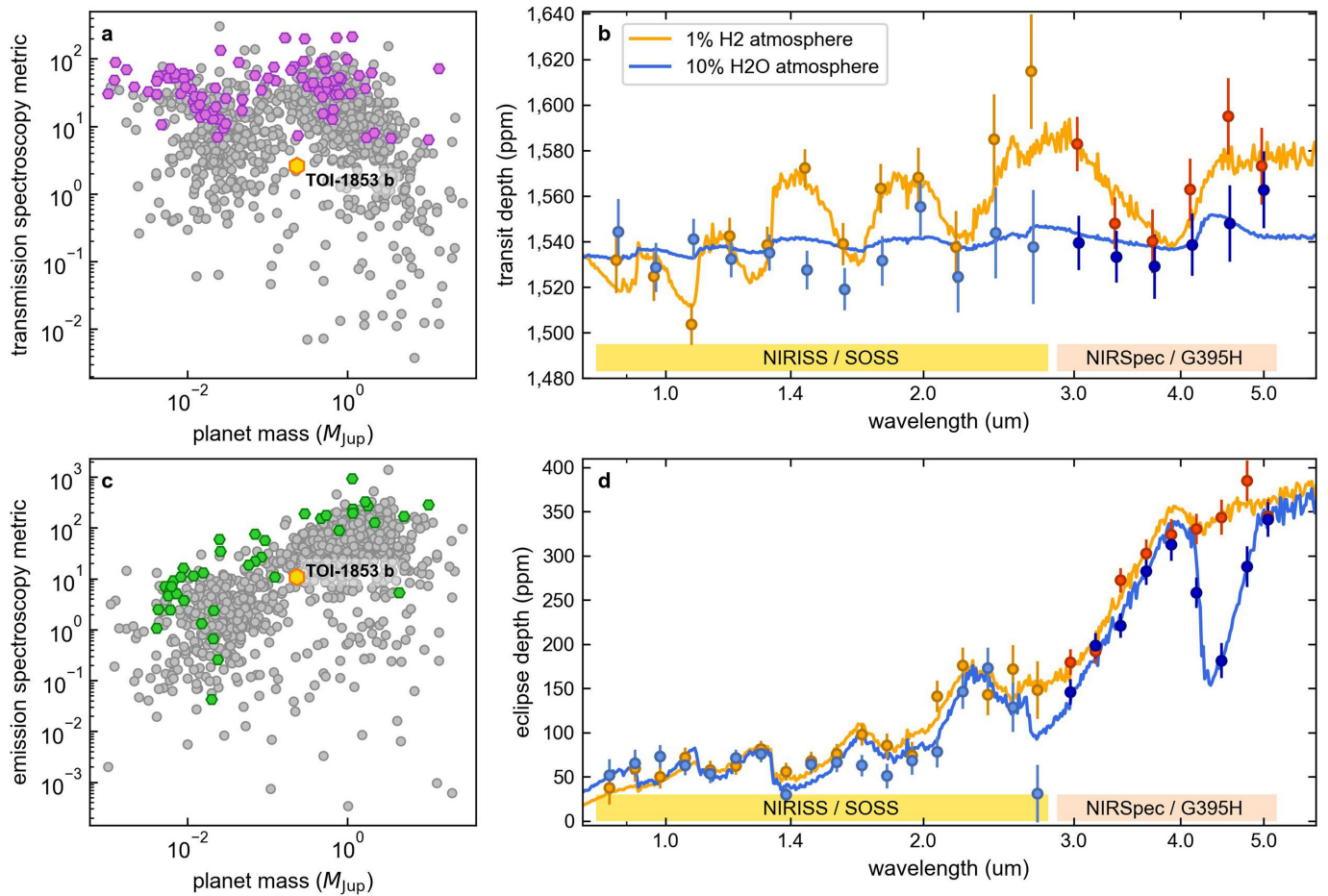
red and green vertical bar, respectively. The horizontal dashed lines mark the 10% and 1% confidence levels (evaluated with the bootstrap method), respectively.



Extended Data Fig. 5 | Corner plot for the posterior distributions of the global joint fit. The blue lines indicate the average value of every parameter and the dashed vertical lines indicate the confidence levels at one standard deviation.



Extended Data Fig. 6 | HARPS-NRV detection map. The colour scale expresses the detection function (for example, the detection probability) and the red circle marks the position of TOI-1853 b.



Extended Data Fig. 7 | Transmission spectroscopy metric, emission spectroscopy metric and simulated spectra for JWST. **a, c** Transit and emission spectroscopic metrics for TOI-1853 b (golden hexagon marker) in comparison with the population of transiting exoplanets (grey markers) and those selected for JWST cycles 1 and 2 observations (purple and green markers). TOI-1853 b has a transmission spectroscopy metric of 2.6 and an

emission spectroscopy metric of 10.9. **b**, Synthetic transmission spectra for an H₂-dominated atmosphere (solid orange line) and an H₂O-dominated atmosphere (solid blue line). The markers with 1σ error bars show simulated JWST observations for selected detectors when combining three transits each. **d**, Same as **b** but for synthetic emission spectra.

Extended Data Table 1 | HARPS-N RVs

BJD _{TDB} (2 459 000 +)	RV (m s ⁻¹)	σ_{RV} (m s ⁻¹)	FWHM	BIS	Contrast	S_{MW}	$\sigma_{S_{MW}}$	BJD _{TDB} (2 459 000 +)	RV (m s ⁻¹)	σ_{RV} (m s ⁻¹)	FWHM	BIS	Contrast	S_{MW}	$\sigma_{S_{MW}}$
277.591475	-26 222.45	3.76	6696	-24	66.70484	0.3101	0.0059	642.724298	-26 306.52	5.95	6692	-61	66.50986	0.328	0.0139
286.743959	-26 310.46	5.20	6658	-37	67.19193	0.2436	0.0096	646.687152	-26 247.78	2.34	6697	-45	66.83894	0.3069	0.0035
288.667942	-26 227.52	3.32	6656	-37	66.92455	0.2719	0.0048	648.731285	-26 318.18	2.81	6682	-47	66.86892	0.2862	0.0049
289.698557	-26 266.06	3.31	6646	-53	66.86836	0.2740	0.0046	649.716835	-26 275.88	3.58	6695	-41	66.83616	0.2651	0.007
297.604184	-26 219.74	6.08	6795	-7	65.98741	0.1466	0.0102	650.721339	-26 223.28	2.49	6665	-35	67.0299	0.3126	0.0042
298.627811	-26 221.87	7.09	6720	-28	66.3382	0.4311	0.0126	656.721298	-26 235.09	6.12	6685	-43	66.52727	0.2212	0.0139
299.645873	-26 263.84	5.51	6748	-42	66.35285	0.3371	0.0086	663.759353	-26 316.48	3.21	6697	-53	66.54938	0.3136	0.0057
305.749103	-26 289.87	4.58	6697	-22	66.60946	0.323	0.0078	678.681216	-26 308.79	5.58	6664	-14	66.59712	0.2085	0.0131
307.671216	-26 251.72	3.43	6743	-39	66.21211	0.3493	0.0041	681.703784	-26 224.39	3.36	6710	-43	66.56025	0.3083	0.0063
325.603943	-26 298.31	7.99	6667	-68	66.49581	0.338	0.0158	682.627666	-26 274.79	2.72	6673	-31	66.80372	0.3234	0.0047
327.671492	-26 280.93	3.56	6757	-32	66.08518	0.2944	0.0045	690.693058	-26 256.22	4.57	6734	-40	66.21964	0.3055	0.0085
360.503076	-26 275.25	5.29	6789	-10	65.92973	0.3035	0.0072	705.597822	-26 243.26	3.76	6706	-38	66.47439	0.3220	0.0069
365.572246	-26 251.83	4.71	6723	-37	66.24472	0.3000	0.0075	706.532481	-26 220.40	3.70	6691	-41	66.80752	0.3202	0.0074
366.609855	-26 304.42	4.00	6734	-47	66.30966	0.2581	0.0064	708.602432	-26 312.25	6.49	6705	-84	66.49706	0.3678	0.0151
367.546558	-26 299.77	3.13	6695	-34	66.79568	0.2893	0.0046	717.556786	-26 253.85	2.14	6692	-37	66.83179	0.3263	0.0029
377.551116	-26 298.75	2.90	6712	-39	66.35716	0.3009	0.0037	718.552650	-26 312.72	2.73	6707	-46	66.61027	0.3156	0.0041
378.532182	-26 245.57	3.57	6735	-41	66.01514	0.2932	0.0047	735.582824	-26 292.60	9.38	6701	-81	66.50634	0.3421	0.0226
379.507227	-26 214.08	4.59	6748	-29	66.11978	0.3012	0.007	737.473873	-26 245.33	22.37	6692	24	65.65718	0.0604	0.0619
387.495223	-26 295.22	3.68	6705	-36	66.52209	0.2931	0.0058	738.528763	-26 284.60	6.08	6694	-37	66.51006	0.3167	0.0134
391.502386	-26 294.81	4.65	6721	-24	66.32581	0.3742	0.0076	748.535890	-26 263.99	6.92	6700	-51	66.38869	0.2286	0.0155
416.441714	-26 288.82	4.19	6683	-37	66.62051	0.2863	0.0069	750.506612	-26 280.71	4.30	6717	-33	66.28337	0.2809	0.0075
565.753307	-26 264.28	3.97	6711	-46	66.64815	0.3154	0.0082	751.517693	-26 226.76	3.34	6731	-39	66.26938	0.2608	0.0052
615.721992	-26 215.50	4.33	6621	-38	67.06423	0.2632	0.0093	752.506892	-26 224.75	3.67	6685	-40	66.58633	0.2531	0.007
617.727567	-26 316.77	7.21	6700	-65	66.12045	0.2601	0.0156	773.458642	-26 265.04	2.74	6693	-48	66.6854	0.3202	0.0042
618.719631	-26 291.42	6.31	6703	-48	66.26545	0.2636	0.0138	774.449876	-26 319.92	2.21	6662	-56	66.99418	0.3100	0.0033
624.713851	-26 245.94	2.79	6638	-39	67.17890	0.2693	0.005	775.457294	-26 302.74	3.73	6689	-42	66.72325	0.3196	0.0072
625.734802	-26 228.39	3.67	6642	-48	66.95316	0.3119	0.0075	803.398361	-26 236.87	2.73	6656	-32	66.94536	0.2849	0.0047
627.729205	-26 321.39	3.55	6675	-44	66.86213	0.3163	0.0069	807.396243	-26 223.01	4.48	6705	-38	66.42269	0.2925	0.0095

FWHM is the full width at half maximum of the cross-correlation function profile, BIS is the bisector inverse slope span, contrast refers to the stellar line measurement of the spectral lines and S_{MW} is the Mount Wilson index.

Extended Data Table 2 | Global joint fit priors and posteriors

Parameters	Unit	Prior distribution	Posterior Value ($\pm 1\sigma$)
<i>RV Parameters</i>			
K_p	m s^{-1}	$\mathcal{U}(0.0, 100.0)$	$48.8^{+1.1}_{-1.0}$
$\bar{\gamma}_{\text{HARPS-N}}$	m s^{-1}	$\mathcal{U}(-26280, -26250)$	$-26267.0^{+0.7}_{-0.6}$
$\sigma_{\text{HARPS-N}}$	m s^{-1}	$\mathcal{U}(0, 10)$	4.8 ± 0.6
<i>Keplerian Parameters</i>			
P	days	$\mathcal{N}(1.24, 0.01)$	1.2436258 ± 0.0000015
T_0	BJD_{TDB}	$\mathcal{N}(2459690.7, 0.1)$	2459690.7420 ± 0.0006
$\sqrt{e} \sin \omega$		$\mathcal{U}(-1.0, 1.0)$	$0.014^{+0.087}_{-0.095}$
$\sqrt{e} \cos \omega$		$\mathcal{U}(-1.0, 1.0)$	$0.053^{+0.053}_{-0.060}$
ρ_*	kg m^{-3}	$\mathcal{N}(2240, 150)$	2236^{+120}_{-114}
<i>Transit Parameters</i>			
r_1		$\mathcal{U}(0.0, 1.0)$	$0.681 \pm^{+0.027}_{-0.027}$
r_2		$\mathcal{U}(0.0, 1.0)$	$0.0392 \pm^{+0.0007}_{-0.0007}$
<i>Limb-darkening coefficients</i>			
q_1 , TESS		$\mathcal{N}(0.40, 0.25)$	$0.36^{+0.13}_{-0.12}$
q_2 , TESS		$\mathcal{N}(0.34, 0.30)$	$0.38^{+0.23}_{-0.21}$
q_1 , LCOGT		$\mathcal{U}(0, 1)$	$0.57^{+0.23}_{-0.25}$
q_2 , LCOGT		$\mathcal{U}(0, 1)$	$0.67^{+0.21}_{-0.25}$
q_1 , ULMT		$\mathcal{U}(0, 1)$	$0.66^{+0.22}_{-0.26}$
q_2 , ULMT		$\mathcal{U}(0, 1)$	$0.47^{+0.28}_{-0.29}$
q_1 , MuSCAT2-g		$\mathcal{U}(0, 1)$	$0.59^{+0.24}_{-0.29}$
q_2 , MuSCAT2-g		$\mathcal{U}(0, 1)$	$0.58^{+0.26}_{-0.28}$
q_1 , MuSCAT2-r		$\mathcal{U}(0, 1)$	$0.52^{+0.27}_{-0.26}$
q_2 , MuSCAT2-r		$\mathcal{U}(0, 1)$	$0.51^{+0.26}_{-0.28}$
q_1 , MuSCAT2-i		$\mathcal{U}(0, 1)$	$0.57^{+0.21}_{-0.24}$
q_2 , MuSCAT2-i		$\mathcal{U}(0, 1)$	$0.42^{+0.29}_{-0.25}$
q_1 , MuSCAT2-z		$\mathcal{U}(0, 1)$	$0.31^{+0.33}_{-0.22}$
q_2 , MuSCAT2-z		$\mathcal{U}(0, 1)$	$0.36^{+0.29}_{-0.23}$
<i>Offset</i>			
off, TESS (Sect. 23)		$\mathcal{N}(0, 0.01)$	$0.00009^{+0.00039}_{-0.00033}$
off, TESS (Sect. 50)		$\mathcal{N}(0, 0.01)$	0.0003 ± 0.0003
off, LCOGT		$\mathcal{N}(0, 0.1)$	$0.005^{+0.030}_{-0.017}$
off, ULMT		$\mathcal{N}(0, 0.1)$	$0.006^{+0.033}_{-0.012}$
off, MuSCAT2-g		$\mathcal{N}(0, 0.1)$	$0.0006^{+0.019}_{-0.012}$
off, MuSCAT2-r		$\mathcal{N}(0, 0.1)$	$0.002^{+0.019}_{-0.005}$
off, MuSCAT2-i		$\mathcal{N}(0, 0.1)$	$0.002^{+0.006}_{-0.015}$
off, MuSCAT2-z		$\mathcal{N}(0, 0.1)$	$-0.005^{+0.012}_{-0.029}$
<i>Jitter</i>			
jitt, TESS (Sect. 23)	ppm	$\mathcal{L}(10^{-1}, 10^5)$	$0.09^{+4.20}_{-0.09}$
jitt, TESS (Sect. 50)	ppm	$\mathcal{L}(10^{-1}, 10^5)$	$0.02^{+1.7}_{-0.02}$
jitt, LCOGT	ppm	$\mathcal{L}(10^{-1}, 10^5)$	55^{+640}_{-55}
jitt, ULMT	ppm	$\mathcal{L}(10^{-1}, 10^5)$	1^{+39}_{-1}
jitt, MuSCAT2-g	ppm	$\mathcal{L}(10^{-1}, 10^5)$	3^{+190}_{-3}
jitt, MuSCAT2-r	ppm	$\mathcal{L}(10^{-1}, 10^5)$	$0.3^{+4.6}_{-0.2}$
jitt, MuSCAT2-i	ppm	$\mathcal{L}(10^{-1}, 10^5)$	14^{+169}_{-13}
jitt, MuSCAT2-z	ppm	$\mathcal{L}(10^{-1}, 10^5)$	39^{+261}_{-37}
<i>Hyper-parameters of the Matern GP model</i>			
σ_{GP} , TESS		$\mathcal{L}(10^{-6}, 0.1)$	$0.00069^{+0.00028}_{-0.00016}$
ρ_{GP} , TESS	days	$\mathcal{L}(0.1, 100)$	$3.9^{+1.4}_{-0.9}$

The best-fitting values and uncertainties are extracted from the posterior probability distributions. $\mathcal{U}(a, b)$ indicates a uniform distribution between a and b , $\mathcal{L}(a, b)$ a log-normal distribution and $\mathcal{N}(a, b)$ a normal distribution with mean a and standard deviation b . The limb-darkening coefficients are intended for a quadratic limb-darkening law.

Extended Data Table 3 | Impact simulation results

id	I:R	$M_{\text{targ}}/M_{\oplus}$	$M_{\text{imp}}/M_{\oplus}$	V_{imp} [km s ⁻¹]	$V_{\text{imp}}/V_{\text{esc}}$	b	M_{Ir}/M_{\oplus}	f_{Si}	$f_{\text{H}_2\text{O}}$	$f_{\text{H\&He}}$	$X_{\text{loss}}^{\text{atmos}}$
1	3:1	25	25	32.6	1.0	0.0	49.4	22.65%	68.15%	9.20%	9.7%
2	3:1	25	25	32.6	1.0	0.4	49.79	22.49%	67.69%	9.82%	2.9%
3	3:1	25	25	32.6	1.0	0.7	49.9	22.43%	67.51%	10.06%	0.3%
4	3:1	25	25	48.9	1.5	0.4	47.8	23.24%	70.25%	6.31%	40.2%
5	1:1	25	25	33.8	1.0	0.0	49.51	45.21%	45.40%	9.39%	7.3%
6	1:1	25	25	33.8	1.0	0.4	49.68	45.06%	45.25%	9.69%	4.2%
7	1:1	25	25	33.8	1.0	0.7	49.86	44.89%	45.08%	10.03%	4.0%
8	1:1	25	25	50.7	1.5	0.4	47.53	47.10%	46.60%	6.30%	40.3%
9	1:3	25	25	34.2	1.0	0.0	49.27	69.29%	22.78%	8.93%	12.1%
10	1:3	25	25	34.2	1.0	0.4	49.61	67.82%	22.61%	9.57%	5.2%
11	1:3	25	25	34.2	1.0	0.7	49.86	67.49%	22.52%	9.99%	0.5%
12	1:3	25	25	51.3	1.5	0.4	47.56	70.74%	22.76%	6.50%	38.25%
13	3:1	60	30	63.0	1.5	0	85.0	23.74%	71.24%	5.02%	52.7%
14	1:1	60	30	64.8	1.5	0	82.8	48.65%	46.65%	4.70%	56.7%
15	1:3	60	30	73.5	1.5	0	82.3	73.63%	20.89%	5.48%	49.8%
16	3:1	60	30	75.5	1.8	0	74.2	27.20%	71.67%	1.13%	90.7%
17	1:1	60	30	77.7	1.8	0	72.8	55.30%	42.92%	1.78%	85.6%
18	1:3	60	30	80.2	1.8	0	73.5	81.11%	16.13%	2.76%	77.4%

Parameters and results for selected impact simulations. I:R represents the mass ratio of ice versus rock in a pre-impact planet: I:R=3:1 refers to water-rich planets, I:R=1:1 refers to equal water and rock planets and I:R=1:3 refers to rock-rich planets. The targets and impactors in each simulation have the same I:R ratio. V_{esc} is the mutual escape velocity in the corresponding impact simulation. M_{c} is the mass of the largest post-collision remnant. f shows the mass ratio of each material in the largest post-collision remnant. $X_{\text{loss}}^{\text{atmos}}$ shows the total mass fraction of the atmosphere that is lost. b is the impact parameter, which is related to the impact angle ($b=0.0$ stands for a head-on impact, $b=0.4$ and 0.7 stand for oblique impacts with impact angles of around 23.6° and 45°, respectively).